Computers and Structures 112–113 (2012) 311–326

Contents lists available at SciVerse ScienceDirect

Computers and Structures

journal homepage: www.elsevier.com/locate/compstruc

A stress improvement procedure

Daniel Jose Payen, Klaus-Jürgen Bathe *

Department of Mechanical Engineering, Massachusetts Institute of Technology, Cambridge, MA 02139, USA

ARTICLE INFO

Article history:
Received 9 April 2012
Accepted 17 July 2012
Available online 15 September 2012

Keywords:
Finite element stress calculation
Low-order displacement-based elements
Stress recovery
Stress convergence
Mixed method
Error measures

ABSTRACT

In this paper, we present a novel procedure to improve the stress predictions in static, dynamic and nonlinear analyses of solids. We focus on the use of low-order displacement-based finite elements – 3-node and 4-node elements in two-dimensional (2D) solutions, and 4-node and 8-node elements in 3D solutions – because these elements are computationally efficient provided good stress convergence is obtained. We give a variational basis of the new procedure and compare the scheme, and its performance, with other effective previously proposed stress improvement techniques. We observe that the stresses of the new procedure converge quadratically in 1D and 2D solutions, i.e. with the same order as the displacements, and conclude that the new procedure shows much promise for the analysis of solids, structures and multiphysics problems, to calculate improved stress predictions and to establish error measures.

© 2012 Elsevier Ltd. All rights reserved.

1. Introduction

During the last decades, many different stress improvement procedures have been explored [1–27]. The aim is to reach enhanced stress predictions, as part of the solution of the mathematical models, and to establish solution error estimates [3,4]. If an effective scheme to enhance the stress predictions were available, the finite element method could be used with coarser meshes, reducing the expense of analysis. Furthermore, an effective scheme to assess the error would be valuable to assure an adequate solution. Early procedures were based either on stress smoothing [5,6] or L_2 projection techniques [7]; however, these approaches are not particularly effective and they have hardly been used in practice.

Considering inexpensive solution error indicators, the stress band plots proposed by Sussman and Bathe [1,8–10] have been used extensively, both for linear and nonlinear analyses, but of course these only give an indication of the solution accuracy – they do not improve the stress predictions.

The calculation of improved stress predictions is particularly important if low-order elements are to be used. For example, considering three-dimensional (3D) solutions, the use of 4-node constant strain tetrahedral elements would frequently be computationally efficient if the stresses could be predicted to a higher accuracy than given directly by the displacements. That is, the constant stress assumption, implied by the assumed linear displacements, is not good in many analyses.

A widely-recognised contribution towards a stress improvement procedure was published by Zienkiewicz and Zhu, when they proposed the 'superconvergent patch recovery' method [11]. This technique is based on the existence of superconvergent points, also referred to as Barlow points [12], where the stresses are of one order higher accuracy than at any other point in the element domain. Appropriate order polynomials approximating the stresses are smoothly fitted through these points, sometimes in a least squares sense. Later, variants of the original method were developed to further enhance its performance [13–15].

Although the superconvergent patch recovery methods seemed to work relatively well for certain elements, superconvergent points do not always exist – e.g. in triangular elements, distorted isoparametric elements and in elements with varying material properties (hence nonlinear analyses) – see the discussion by Hiller and Bathe [16]. Three widely used procedures that do not require the knowledge of superconvergent points are the 'posterior equilibrium method' (PEM), the 'recovery by equilibrium in patches' (REP) method, and the 'recovery by compatibility in patches' (RCP) method.

The PEM was proposed by Stein and Ohnimus [17] and is based on the work published earlier by Stein and Ahmad [18,19]. This method uses the principle of virtual work to calculate improved interelement tractions for the purposes of local error estimation [17,20]. The REP method was proposed by Boroomand and Zienkiewicz [21,22]. This method uses the principle of virtual work to calculate improved stresses within the finite element domain. The RCP method was proposed by Ubertini [23] and further developed by Benedetti et al. [24]. This method uses the principle of minimum complementary energy to calculate improved stresses that satisfy point-wise equilibrium. Later, Castellazzi et al.

* Corresponding author.
E-mail address: kjb@mit.edu (K.J. Bathe).

0045-7949/$ - see front matter © 2012 Elsevier Ltd. All rights reserved.
http://dx.doi.org/10.1016/j.compstruc.2012.07.006

established a solution error estimate based on the RCP method to guide adaptive meshing [25].

All three stress calculation procedures yield impressive results that exceed the performance of the superconvergent patch recovery method. However, to ensure a well-posed problem for the solution of the unknown stress coefficients, several assumptions are employed, and these assumptions limit the accuracy of the results. Specifically, the PEM assumes that the improved interelement tractions are approximately equal (by a difference minimization) to the tractions directly-calculated from the displacement solution [17]; the REP method uses element nodal point forces that correspond to individual stress components [22]; and the RCP method imposes differential equilibrium for all points in the element [24], a constraint which is too severe, as a result the RCP solution is not reliable for all classes of problems.

Recently, we proposed the NPF-based method [26,27]. This procedure also employs the principle of virtual work, but without the assumptions used in the earlier methods. While the numerical results in Refs. [26,27] are encouraging, the method still requires to consider specific element stress domains and some stress averaging. We concluded, see Refs. [26,27], that a variational basis was necessary to obtain further insight and possibly improve the schemes.

For various problems in engineering and the sciences – like in the analysis of (almost) incompressible media, thin structures, and multiphysics phenomena – optimal finite element discretisations can only be obtained if mixed variational formulations are used [1,28–34]. Indeed, in Ref. [35], Mota and Abel show that the stress smoothing, L_2 projection and superconvergent patch recovery techniques are based on the use of the Hu-Washizu principle.

Our objective in this paper is to show that the PEM and the REP, RCP, and NPF-based methods are also all based, with certain assumptions, on the Hu-Washizu variational principle, and then present a novel and significantly improved procedure for stress predictions. Throughout we focus on the use of low-order displacement-based finite element discretisations of solids, that is, 2-node elements in 1D solutions, 3-node triangular and 4-node quadrilateral elements in 2D solutions, and 4-node tetrahedral and 8-node brick elements in 3D solutions. These elements are computationally efficient provided good stress convergence is obtained.

We analyse the new stress prediction procedure in detail for 1D problems using 2-node elements with arbitrary loading and material properties (but constant cross-sectional area), and prove that the procedure is reliable, giving stresses that are, in fact, optimal stress predictions (in the norm used), with the order of convergence being quadratic, i.e. the same order as for the displacements. This order of stress convergence is also seen numerically in 1D and 2D solutions. In a study, we compare the performance of the new method with the other above-mentioned procedures (that is, with the best stress improvement procedures currently available). It is important to note that we consider static, dynamic and nonlinear solutions. Throughout the paper we use the notation of Ref. [1].

2. Fundamental equations

Consider the equilibrium of a body of volume V and surface area S, subjected to externally applied surface tractions $\underline{f}^S$ on the area S_f and body forces $\underline{f}^B$; see Fig. 1. The body is supported on the area S_u with prescribed displacements $\underline{u}_p$, and, for now, linear analysis conditions are assumed. We seek to calculate the unknown displacements, strains and stresses.

In the differential formulation of the problem, the unknown response is calculated by solving the governing differential equations of equilibrium and compatibility, with the constitutive relationships, subject to the applied boundary conditions. That is, we solve

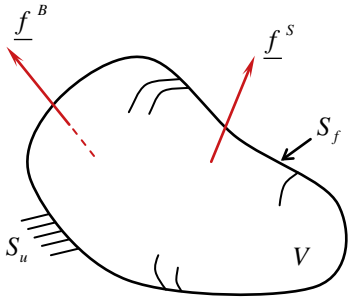

Fig. 1. General 3D body of volume V and surface area S, where $S_u \cup S_f = S$ and $S_u \cap S_f = 0$.

$$div[\underline{\tau}_{ex}] + \underline{f}^B = \underline{0}$$

$$\underline{\varepsilon}_{ex} = \partial_\varepsilon \underline{u}_{ex}$$

$$\underline{\tau}_{ex} = \underline{C}\ \underline{\varepsilon}_{ex}$$

subject to

$$\underline{u}_{ex} = \underline{u}_p \quad on\ S_u$$
$$\underline{f}^S = \underline{\tau}_{ex}\underline{n} \quad on\ S_f$$

where $\underline{u}_{ex}$, $\underline{\varepsilon}_{ex}$ and $\underline{\tau}_{ex}$ are the exact displacements, strains and stresses, respectively, ∂_ε is the differential operator on $\underline{u}_{ex}$ to obtain the strain components $\underline{\varepsilon}_{ex}$, $\underline{C}$ is the stress–strain matrix, and $\underline{n}$ is the unit outward normal vector on the surface S_f.

A second (but entirely equivalent) approach to the solution of the problem is given by minimising the total potential energy $\Pi(\underline{u})$,

$$\Pi(\underline{u}) = \int_V \frac{1}{2}\underline{\varepsilon}^T\underline{\tau}\ dV - \int_{S_f}\underline{u}^T\underline{f}^S\ dS - \int_V \underline{u}^T\underline{f}^B\ dV \tag{1}$$

with the constraints

$$\begin{aligned}&\underline{\varepsilon} = \partial_\varepsilon \underline{u}\\ &\underline{\tau} = \underline{C}\ \underline{\varepsilon}\\ &\underline{u} = \underline{u}_p\ on\ S_u\end{aligned} \tag{2}$$

where $\underline{u}$ is any displacement field satisfying the boundary condition on S_u, and $\underline{\varepsilon}$ and $\underline{\tau}$ are the strains and stresses corresponding to $\underline{u}$.

For approximate solutions, a larger class of trial functions can be employed when we operate on the total potential energy rather than on the differential formulation of the problem; see Refs. [1,10]. This has important consequences and much of the success of the finite element method hinges on this fact.

3. Finite element methods for stress predictions

In this section, we first review the displacement-based finite element method, then we present a mixed formulation based on the Hu-Washizu principle. Thereafter, we specialise this mixed formulation to arrive at the basic equations of the PEM and the REP, RCP, and NPF-based methods. Finally, we use this mixed formulation – and its properties – to present our new stress prediction scheme.

3.1. Displacement-based finite element method

In the displacement-based finite element method, we assume a displacement pattern within each element m, that is, $\underline{u}^{(m)} = \underline{H}^{(m)}\widehat{\underline{U}}$, where $\underline{H}^{(m)}$ is the displacement interpolation matrix and $\widehat{\underline{U}}$ lists the nodal point displacements of the assemblage (including those at the supports).

With this assumption, the strains $\underline{\varepsilon}^{(m)}$ and stresses $\underline{\tau}_h^{(m)}$ of element m follow directly from Eq. (2),

$$\underline{\varepsilon}^{(m)} = \underline{\partial}_\varepsilon \underline{u}^{(m)} = \underline{B}^{(m)} \widehat{\underline{U}} \tag{3}$$

$$\underline{\tau}_h^{(m)} = \underline{C}^{(m)} \underline{\varepsilon}^{(m)} = \underline{C}^{(m)} \underline{B}^{(m)} \widehat{\underline{U}} \tag{4}$$

Then, minimising Π of Eq. (1) yields

$$\left[\sum_{m=1}^{N} \left(\int_{V^{(m)}} \underline{B}^{(m)T} \underline{C}^{(m)} \underline{B}^{(m)} \, dV \right)\right] \widehat{\underline{U}} = \left\{ \sum_{m=1}^{N} \left(\int_{S_f^{(m)}} \underline{H}^{(m)T} \underline{f}^S \, dS + \int_{V^{(m)}} \underline{H}^{(m)T} \underline{f}^B \, dV \right) \right\} \tag{5}$$

where $\underline{B}^{(m)}$, $\underline{C}^{(m)}$, $V^{(m)}$, and $S_f^{(m)}$ are the strain–displacement matrix, the stress–strain matrix, the volume, and the surface area with externally applied tractions of element m, respectively. We sum over all N elements in the mesh and use Eq. (5) to obtain $\widehat{\underline{U}}$; see for example Ref. [1]. Finally, $\underline{\tau}_h^{(m)}$ is calculated using Eq. (4).

In the following, we focus on the use of low-order finite element discretisations (the 2-node element in 1D solutions, the 3-node and 4-node elements in 2D solutions, etc.). It is well known that the accuracy of $\underline{\tau}_h^{(m)}$ is then poor, as compared with the accuracy of the calculated displacements, and this deficiency can be seen using stress band plots of unsmoothed stresses [1,8–10]. We refer to these stresses as the "directly-calculated finite element stresses".

3.2. Mixed formulation

To arrive at accurate stress predictions, a mixed interpolation approach – which can be thought of as a special use of the Hu-Washizu principle – can be more effective. In this formulation, rather than applying the stress–strain relationship point-wise, we relax this relationship and apply it over the element volumes using Lagrange multipliers. The primary solution variables are then the unknown displacements, Lagrange multipliers and stresses. Hence, the equivalent of the minimisation of Π in Eq. (1) is

$$\Pi^*(\underline{u}^{(m)}, \underline{\lambda}^{(m)}, \underline{\tau}^{(m)}) = \sum_{m=1}^{N} \left(\int_{V^{(m)}} \frac{1}{2} \underline{\varepsilon}^{(m)T} \underline{\tau}^{(m)} \, dV - \int_{S_f^{(m)}} \underline{u}^{(m)T} \underline{f}^S \, dS - \int_{V^{(m)}} \underline{u}^{(m)T} \underline{f}^B \, dV - \int_{V^{(m)}} \underline{\lambda}^{(m)T} \{ \underline{\tau}^{(m)} - \underline{C}^{(m)} \underline{\varepsilon}^{(m)} \} \, dV \right) = \text{stationary} \tag{6}$$

with the constraints

$$\begin{aligned} &\underline{\varepsilon}^{(m)} = \underline{\partial}_\varepsilon \underline{u}^{(m)} \\ &\underline{u}^{(m)} = \underline{u}_p \quad \text{on } S_u \end{aligned} \tag{7}$$

As in the displacement-based finite element method, the displacements $\underline{u}^{(m)}$ of element m are defined by nodal point variables that pertain to adjacent elements in the assemblage, $\underline{u}^{(m)} = \underline{H}^{(m)} \widehat{\underline{U}}$, and the strains $\underline{\varepsilon}^{(m)}$ follow directly from Eq. (7), $\underline{\varepsilon}^{(m)} = \underline{B}^{(m)} \widehat{\underline{U}}$. However, the Lagrange multipliers $\underline{\lambda}^{(m)}$ and the stresses $\underline{\tau}^{(m)}$ of element m are defined by internal degrees of freedom that pertain only to the specific element m considered.

In order to furnish improved stress predictions, we must assume a richer space for $\underline{\tau}^{(m)}$ than that implicitly assumed for $\underline{\tau}_h^{(m)}$. Also, we want to enhance the fulfilment of equilibrium. Hence, we now assume

$$dim(\underline{\tau}^{(m)}) \geqslant dim(\underline{\lambda}^{(m)}) \geqslant dim(\underline{\varepsilon}^{(m)}) \tag{8}$$

and

$$\int_{V^{(m)}} \delta \underline{\zeta}^{(m)T} \left\{ div[\underline{\tau}^{(m)}] + \underline{f}^B \right\} dV = 0 \tag{9}$$

where *dim* (.) denotes the dimension of the space of the variable considered, δ denotes, as usual, "variation of", $\underline{\zeta}^{(m)}$ is an element of a space discussed below (the space depends on the method used), and the square parentheses indicate that the stress vector has been arranged into matrix form.

With this assumption, invoking the stationarity of Π^* with respect to $\underline{u}^{(m)}$, $\underline{\lambda}^{(m)}$ and $\underline{\tau}^{(m)}$ yields

$$\sum_{m=1}^{N} \left(\int_{V^{(m)}} \delta \underline{\varepsilon}^{(m)T} \left\{ \frac{1}{2} \underline{\tau}^{(m)} + \underline{C}^{(m)} \underline{\lambda}^{(m)} \right\} dV - \int_{S_f^{(m)}} \delta \underline{u}^{(m)T} \underline{f}^S \, dS - \int_{V^{(m)}} \delta \underline{u}^{(m)T} \underline{f}^B \, dV \right) = 0 \tag{10}$$

$$\int_{V^{(m)}} \delta \underline{\lambda}^{(m)\,T} \{ \underline{\tau}^{(m)} - \underline{C}^{(m)} \underline{\varepsilon}^{(m)} \} \, dV = 0 \quad \forall \; m \tag{11}$$

$$\underline{\lambda}^{(m)} = \frac{1}{2} \underline{\varepsilon}^{(m)} \quad \forall \quad m \tag{12}$$

Since Eq. (11) holds for all variations of $\underline{\lambda}^{(m)}$, including when $\delta \underline{\lambda}^{(m)} = \frac{1}{2} \delta \underline{\varepsilon}^{(m)}$, Eq. (10) contains as a special case

$$\sum_{m=1}^{N} \left(\int_{V^{(m)}} \delta \underline{\varepsilon}^{(m)T} \left\{ \frac{1}{2} \underline{C}^{(m)} \underline{\varepsilon}^{(m)} + \underline{C}^{(m)} \underline{\lambda}^{(m)} \right\} dV - \int_{S_f^{(m)}} \delta \underline{u}^{(m)T} \underline{f}^S \, dS - \int_{V^{(m)}} \delta \underline{u}^{(m)T} \underline{f}^B \, dV \right) = 0$$

Then, using the solution $\underline{\lambda}^{(m)} = \frac{1}{2} \underline{\varepsilon}^{(m)}$ from Eq. (12) we obtain

$$\sum_{m=1}^{N} \left(\int_{V^{(m)}} \delta \underline{\varepsilon}^{(m)T} \underline{C}^{(m)} \underline{\varepsilon}^{(m)} \, dV - \int_{S_f^{(m)}} \delta \underline{u}^{(m)T} \underline{f}^S \, dS - \int_{V^{(m)}} \delta \underline{u}^{(m)T} \underline{f}^B \, dV \right) = 0 \tag{13}$$

Of course, when inserting the element interpolations, Eq. (13) gives Eq. (5). Here Eq. (13) (and hence Eq. (5)) would give – at this stage – a specific solution of the stresses in the stress space of $\underline{\tau}^{(m)}$, namely $\underline{\tau}_h^{(m)}$. However, to complete the calculation of the improved stresses we also use Eqs. (9) and (11).

An important practical feature of this 'mixed formulation' is that the displacement problem in Eq. (13) is decoupled from the additional calculations of the stresses. Therefore, in a general analysis, we first solve for $\underline{u}^{(m)}$ as is standard, and then – rather than applying the stress–strain relationship – we obtain $\underline{\tau}^{(m)}$ from $\underline{u}^{(m)}$ by applying Eqs. (9) and (11) to *each* element m in the assemblage.

This element-based approach works well in 1D solutions; however, in 2D and 3D solutions, better results are obtained when the stresses are defined over a predetermined patch of N_P elements known as the stress calculation domain. In this case, $\underline{\tau}^{(m)}$ is obtained from $\underline{u}^{(m)}$ by applying Eqs. (9) and (11) either to each element m in the stress calculation domain, or to the *entire* stress calculation domain,

$$\sum_{m=1}^{N_P} \left(\int_{V^{(m)}} \delta \underline{\lambda}^{(m)T} \{ \underline{\tau}^{(m)} - \underline{C}^{(m)} \underline{\varepsilon}^{(m)} \} dV \right) = 0 \tag{14}$$

$$\sum_{m=1}^{N_P} \left(\int_{V^{(m)}} \delta \underline{\zeta}^{(m)T} \{ div[\underline{\tau}^{(m)}] + \underline{f}^B \} dV \right) = 0 \tag{15}$$

Since $\underline{\tau}^{(m)}$ is obtained from $\underline{u}^{(m)}$, the accuracy of $\underline{\tau}^{(m)}$ is limited by that of $\underline{u}^{(m)}$; hence, the highest order of convergence of the stresses that we can expect is $O(h^2)$ in the H^0 norm (that is, in the L^2 norm) – one order higher than that observed for $\underline{\tau}_h^{(m)}$.

The key question for the formulation is now: What interpolations should be used for $\underline{\lambda}^{(m)}$ and $\underline{\zeta}^{(m)}$ to ensure a well-posed problem with stresses that converge at order $O(h^2)$? Indeed, the choice of interpolation determines the number of equations available and the accuracy of the results. Examples are given below.

3.3. The PEM and the REP method

In the PEM and the REP method, $\underline{\lambda}^{(m)}$ is interpolated in the same way as the strains $\underline{\varepsilon}^{(m)}$ and $\underline{\zeta}^{(m)}$ is interpolated in the same way as the displacements $\underline{u}^{(m)}$. With this assumption, we obtain from Eqs. (14) and (15)

$$\sum_{m=1}^{N_p}\left(\int_{V^{(m)}}\delta\underline{\varepsilon}^{(m)T}\underline{\tau}^{(m)}dV\right)=\sum_{m=1}^{N_p}\left(\delta\widehat{\underline{U}}^T\underline{F}^{(m)}\right) \tag{16}$$

$$\sum_{m=1}^{N_p}\left(\int_{V^{(m)}}\delta\underline{u}^{(m)T}\left\{div[\underline{\tau}^{(m)}]+\underline{f}^B\right\}dV\right)=0 \tag{17}$$

where $\delta\widehat{\underline{U}}$ are the virtual nodal point displacements that correspond to $\delta\underline{\varepsilon}^{(m)}$ and $\underline{F}^{(m)}$ are the element nodal point forces, in fact already used in Eq. (5),

$$\underline{F}^{(m)}=\int_{V^{(m)}}\underline{B}^{(m)T}\underline{\tau}_h^{(m)}dV=\left[\int_{V^{(m)}}\underline{B}^{(m)T}\underline{C}^{(m)}\underline{B}^{(m)}dV\right]\widehat{\underline{U}} \tag{18}$$

Using the mathematical identity $\delta\underline{u}^{(m)T}div[\underline{\tau}^{(m)}]=div(\delta\underline{u}^{(m)T}[\underline{\tau}^{(m)}])-\delta\underline{\varepsilon}^{(m)T}\underline{\tau}^{(m)}$, the Gauss divergence theorem and Eq. (16), we can write Eq. (17) as

$$\sum_{m=1}^{N_p}\left(\int_{S_f^{(m)}}\delta\underline{u}^{(m)T}[\underline{\tau}^{(m)}]\underline{n}^{(m)}dS+\int_{V^{(m)}}\delta\underline{u}^{(m)T}\underline{f}^B dV\right)=\sum_{m=1}^{N_p}\left(\delta\widehat{\underline{U}}^T\underline{F}^{(m)}\right) \tag{19}$$

where $\underline{n}^{(m)}$ is the unit normal to the boundary surface $S_f^{(m)}$ of element m.

Eq. (19) is the basic equation of the PEM and Eq. (16) is the basic equation of the REP method. That is, for any virtual displacement pattern contained in the interpolation functions, the PEM balances the virtual work of the boundary tractions (adjusted for body force effects) with the virtual work of the nodal point forces, whereas the REP method balances the internal virtual work of the stresses with the virtual work of the nodal point forces.

Since each method uses only one principle of virtual work statement (of the two possible statements given by the mixed formulation), the governing matrices corresponding to the basic equations of the PEM and the REP method may be singular; hence, several assumptions are employed to add extra constraints (and these assumptions limit the accuracy of the results) – see Refs. [17,22].

3.4. The RCP method

Let V^τ be the assumed stress space for $\underline{\tau}^{(m)}$, and let $\bar{\mathrm{V}}^\tau$ be the subspace of the self-equilibrated stresses in V^τ. Then, let $\bar{\underline{\tau}}^{(m)}$ be any element in that subspace

$$\bar{\mathrm{V}}^\tau=\left\{\bar{\underline{\tau}}^{(m)}\,|\,\bar{\underline{\tau}}^{(m)}\in\mathrm{V}^\tau;div\left[\bar{\underline{\tau}}^{(m)}\right]=\underline{0}\right\} \tag{20}$$

In the RCP method, $\underline{\lambda}^{(m)}$ is interpolated in the same way as $\underline{C}^{(m)-1}\bar{\underline{\tau}}^{(m)}$ and $\underline{\zeta}^{(m)}$ is any element in $L^2(V_p)$, where $L^2(V_p)$ is the space of square integrable functions in the volume, V_p, of the stress calculation domain. With this assumption, we obtain from Eqs. (14) and (15)

$$\sum_{m=1}^{N_p}\left(\int_{V^{(m)}}\delta\bar{\underline{\tau}}^{(m)T}\left\{\underline{C}^{(m)-1}\underline{\tau}^{(m)}-\underline{\varepsilon}^{(m)}\right\}dV\right)=0 \tag{21}$$

$$div[\underline{\tau}^{(m)}]+\underline{f}^B=0 \tag{22}$$

Eqs. (21) and (22) are basic equations of the RCP method. To satisfy Eq. (22), an *a priori* particular solution $\underline{\tau}_{p.s.}^{(m)}$ to the differential equations of equilibrium is embedded in $\underline{\tau}^{(m)}$ [23,24]. However, establishing $\underline{\tau}_{p.s.}^{(m)}$ for distorted isoparametric elements in dynamic analysis is difficult and is an outstanding issue to be solved. Moreover, the differential equilibrium constraint in Eq. (22) is too severe, as a result the RCP solution is not reliable for all classes of problems; see section 5.

Considering nonlinear analysis, a complication with the RCP method is that the basic equations involve the use of the constitutive relationships; hence, in problems with path-dependent nonlinear material conditions, an incremental solution procedure may have to be used to solve for the unknown stress coefficients in Eq. (21).

3.5. The NPF-based method

In the NPF-based method, $\underline{\lambda}^{(m)}$ is interpolated in the same way as the strains $\underline{\varepsilon}^{(m)}$ and $\underline{\zeta}^{(m)}$ is interpolated in the same way as the displacements $\underline{u}^{(m)}$. With this assumption we obtain from Eq. (11) and Eq. (9)

$$\int_{V^{(m)}}\delta\underline{\varepsilon}^{(m)T}\underline{\tau}^{(m)}dV=\delta\widehat{\underline{U}}^T\underline{F}^{(m)} \tag{23}$$

$$\int_{V^{(m)}}\delta\underline{u}^{(m)T}\{div[\underline{\tau}^{(m)}]+\underline{f}^B\}dV=0 \tag{24}$$

where $\underline{F}^{(m)}$ is defined in Eq. (18) and, using similar steps as those used to obtain Eq. (19), we can write Eq. (24) as

$$\int_{S_f^{(m)}}\delta\underline{u}^{(m)T}[\underline{\tau}^{(m)}]\underline{n}^{(m)}dS+\int_{V^{(m)}}\delta\underline{u}^{(m)T}\underline{f}^B dV=\delta\widehat{\underline{U}}^T\underline{F}^{(m)} \tag{25}$$

Eqs. (23) and (25) are the basic equations of the NPF-based method. In contrast to the PEM and the REP method, the NPF-based method uses both principle of virtual work statements, Eqs. (23) and (25), and applies them to *each* element m in the stress calculation domain. Consequently, the problem solution for the unknown NPF-based stress coefficients is well-posed without the (limiting) assumptions used in the earlier methods.

However, a drawback of the NPF-based method is that the number of equations available – and hence the dimension of the interpolation functions assumed in V^τ – is dependent on the number (and type) of elements in the stress calculation domain. Therefore, to get close to $O(h^2)$ convergence for the stresses, a large stress domain is needed and a domain stress averaging procedure has been employed; see Refs. [26,27].

3.6. The new stress improvement procedure

In this section, we present a novel and significantly improved procedure for stress predictions. We first develop the method for linear static and dynamic analysis and then we extend the method to nonlinear solutions. Finally, we consider the computational cost of the technique.

3.6.1. Linear static and dynamic analysis

The new stress improvement procedure assumes $\underline{\lambda}^{(m)}$ is interpolated in the same way as the self-equilibrated stresses $\bar{\underline{\tau}}^{(m)}$ and $\underline{\zeta}^{(m)}$ is any element in $P_1(V_p)$, where $P_k(V_p)$ is the space of complete polynomials of degree k in the volume, V_p, of the stress calculation domain. With this assumption, we obtain from Eqs. (14) and (15)

$$\sum_{m=1}^{N_p}\left(\int_{V^{(m)}}\delta\bar{\underline{\tau}}^{(m)T}\left\{\underline{\tau}^{(m)}-\underline{\tau}_h^{(m)}\right\}dV\right)=0 \tag{26}$$

$$\sum_{m=1}^{N_p}\left(\int_{V^{(m)}}\delta\underline{\zeta}^{(m)T}\left\{div[\underline{\tau}^{(m)}]+\underline{f}^B\right\}dV\right)=0 \tag{27}$$

where the stresses $\underline{\tau}^{(m)}$ are assumed to be continuous and quadratically interpolated across the stress calculation domain, $\underline{\tau}^{(m)}\in P_2(V_p)$, and the space of self-equilibrated stresses, $\bar{\mathrm{V}}^\tau$, is given by

$$\bar{V}^{\tau} = \{\bar{\underline{\tau}}^{(m)} \mid \bar{\underline{\tau}}^{(m)} \in P_2(V_p); div[\bar{\underline{\tau}}^{(m)}] = \underline{0}\} \tag{28}$$

Eqs. (26) and (27) are the basic equations used. The first equation, Eq. (26), expresses that the projection of the difference in the enhanced and directly-calculated stresses onto $\bar{V}^{\tau}$ shall be zero. Hence, this condition in essence extracts from $\underline{\tau}_h^{(m)}$ that part which is of good quality. The second equation, Eq. (27), then enforces that the difference in the divergence of the enhanced and the exact stresses in the projection onto the space P_1 is also zero.

To obtain the corresponding finite element equations, we introduce the interpolations

$$\underline{\tau}^{(m)} = \underline{E}_{\tau}\hat{\underline{\tau}}, \quad \bar{\underline{\tau}}^{(m)} = \bar{\underline{E}}_{\tau}\hat{\underline{\tau}}, \quad \underline{\zeta}^{(m)} = \underline{E}_{\zeta}\hat{\underline{\zeta}} \tag{29}$$

where the interpolation matrices $\underline{E}_{\tau}$, $\bar{\underline{E}}_{\tau}$, and $\underline{E}_{\zeta}$ are given in Eq. (35) for 1D analysis, and in Eqs. (45)–(47), respectively, for 2D analysis. Note that in these matrices locally based coordinate origins are used to avoid ill-conditioning, and $div[\bar{\underline{E}}_{\tau}] = \underline{0}$, as is required by Eq. (28).

Substituting from Eq. (29) into Eqs. (26) and (27) we arrive at

$$\left[\sum_{m=1}^{N_P}\begin{pmatrix} \int_{V^{(m)}} \bar{\underline{E}}_{\tau}^T \underline{E}_{\tau} dV \\ \int_{V^{(m)}} \underline{E}_{\zeta}^T \underline{\partial}_{\tau} \underline{E}_{\tau} dV \end{pmatrix}\right]\hat{\underline{\tau}} = \left\{\sum_{m=1}^{N_P}\begin{pmatrix} \int_{V^{(m)}} \bar{\underline{E}}_{\tau}^T \underline{\tau}_h^{(m)} dV \\ -\int_{V^{(m)}} \underline{E}_{\zeta}^T \underline{f}^B dV \end{pmatrix}\right\} \tag{30}$$

where $\underline{\partial}_{\tau}$ is the differential operator on $\underline{\tau}^{(m)}$ to obtain the divergence of the stress field (see Eqs. (36) and (48)), $\hat{\underline{\tau}}$ lists the unknown stress coefficients to be found, and, in dynamic analysis, we must include the d'Alembert inertia forces in $\underline{f}^B$; see section 5.5.

Since $\underline{\tau}^{(m)} \in P_2(V_p)$, and $\bar{\underline{\tau}}^{(m)} \in \bar{V}^{\tau}$, $\underline{\zeta}^{(m)} \in P_1(V_p)$, it follows that Eq. (30) represents a determined system of equations in terms of $\hat{\underline{\tau}}$ – *irrespective* of the number (and type) of elements used in the stress calculation domain – such that a unique solution for $\hat{\underline{\tau}}$ always exists, even if only one element is used in the stress calculation domain.

To summarise, the important attributes of the new method are:

1. The assumed stresses $\underline{\tau}^{(m)}$ are interpolated with complete polynomials of degree 2; hence, the order of convergence of $\underline{\tau}^{(m)}$ is expected to be $O(h^2)$.
2. The number of equations available is independent of the number (and type) of elements used in the stress calculation domain.
3. The system of equations is always determined.
4. The equations do not involve the use of the constitutive relationships (other than in the calculation of $\underline{\tau}_h^{(m)}$).
5. The stress calculations can be performed for the entire assemblage, or just in localised regions of concern.
6. The fulfilment of differential equilibrium is enhanced, and differential equilibrium is fulfilled at every point in the element if $\underline{f}^B \in P_1$.
7. The method does not use an *a priori* particular solution (like used in the RCP method).
8. $\underline{\tau}_h^{(m)}$ can also be established from a mixed formulation (such as the u/p formulation, the incompatible modes formulation, etc.), and the method can still be used to enhance the stress solution.
9. The enhanced stress solution will not be afflicted with a spurious checkerboard mode of constant element stresses.

Spurious checkerboard modes of constant element stresses can be found in some displacement-stress solutions – see Fig. 2 and Ref. [1]. To prove that the improved stresses $\underline{\tau}^{(m)}$ are not afflicted we use Eq. (26) to obtain

$$\sum_{m=1}^{N_P}\left(\int_{V^{(m)}} \underline{\tau}^{(m)} dV\right) = \sum_{m=1}^{N_P}\left(\int_{V^{(m)}} \underline{\tau}_h^{(m)} dV\right) \tag{31}$$

and note that the directly-calculated stresses, $\underline{\tau}_h^{(m)}$, established in a proper formulation (e.g. the displacement formulation), are not afflicted.

+	−	+	−
−	+	−	+
+	−	+	−
−	+	−	+

Fig. 2. Checkerboard mode of constant element stress. Here + and − denote $+\Delta\tau_{ij}^{(m)}$ and $-\Delta\tau_{ij}^{(m)}$, where $\Delta\tau_{ij}^{(m)}$ is an arbitrary value; see Ref. [1].

Also, because the exact stresses satisfy the differential equations of equilibrium, we can write Eq. (27) as

$$\sum_{m=1}^{N_P}\left(\int_{V^{(m)}} \delta\underline{\zeta}^{(m)T} div[\underline{\tau}^{(m)}] dV\right) = \sum_{m=1}^{N_P}\left(\int_{V^{(m)}} \delta\underline{\zeta}^{(m)T} div[\underline{\tau}_{ex}] dV\right) \tag{32}$$

such that

$$\sum_{m=1}^{N_P}\left(\int_{V^{(m)}} div[\underline{\tau}^{(m)}] dV\right) = \sum_{m=1}^{N_P}\left(\int_{V^{(m)}} div[\underline{\tau}_{ex}] dV\right) \tag{33}$$

Eqs. (32) and (33) are important since they relate the calculated and exact stresses in the volume of the stress calculation domain. Indeed, we shall use these relationships when we consider an error bound on $\underline{\tau}^{(m)}$.

Finally, we note that the PEM, and the REP and NPF-based methods satisfy the condition on $\underline{\lambda}^{(m)}$ given in Eq. (8), irrespective of N_P. However, the RCP method and the new method only satisfy this condition when $N_P = 1$ (because these two methods assume $\underline{\lambda}^{(m)}$ to be continuous across element boundaries whereas $\underline{\varepsilon}^{(m)}$ does not show that continuity).

3.6.2. Nonlinear analysis

In nonlinear analyses, all theory presented is applicable, but of course the current volumes and current Cauchy stresses must be used; see Ref. [1]. That is, if t denotes "in the current configuration", the stress coefficients ${}^t\hat{\underline{\tau}}$ are obtained using

$$\left[\sum_{m=1}^{N_P}\begin{pmatrix} \int_{{}^tV^{(m)}} \bar{\underline{E}}_{\tau}^T \underline{E}_{\tau} dV \\ \int_{{}^tV^{(m)}} \underline{E}_{\zeta}^T \underline{\partial}_{\tau} \underline{E}_{\tau} dV \end{pmatrix}\right]{}^t\hat{\underline{\tau}} = \left\{\sum_{m=1}^{N_P}\begin{pmatrix} \int_{{}^tV^{(m)}} \bar{\underline{E}}_{\tau}^T {}^t\underline{\tau}_h^{(m)} dV \\ -\int_{{}^tV^{(m)}} \underline{E}_{\zeta}^T {}^t\underline{f}^B dV \end{pmatrix}\right\} \tag{34}$$

where ${}^tV^m$ is the current volume of element m (obtained from the displacement solution ${}^t\widehat{U}$), ${}^t\underline{\tau}_h^{(m)}$ lists the directly-calculated Cauchy stresses at time t, and ${}^t\widehat{\underline{U}}$ is established using a step-by-step incremental solution procedure [1].

Therefore, once ${}^t\widehat{\underline{U}}$ has been established, the enhanced stress predictions are obtained using Eq. (34), as in linear analysis.

3.6.3. Computational expense

The computational expense to furnish improved stress predictions is given by the numerical effort involved in solving for 18 unknown stress coefficients in 2D solutions (and the 60 unknown stress coefficients in 3D solutions) for each element m where stresses are to be improved.

This expense is small, compared with factorising the global stiffness matrix. Indeed, the expense to enhance the stresses for the *entire* assemblage in a typical linear static analysis problem (with 10^5 to 10^6 degrees of freedom) is probably only about 1% of the total solution cost. In nonlinear analyses the expense is, rel-

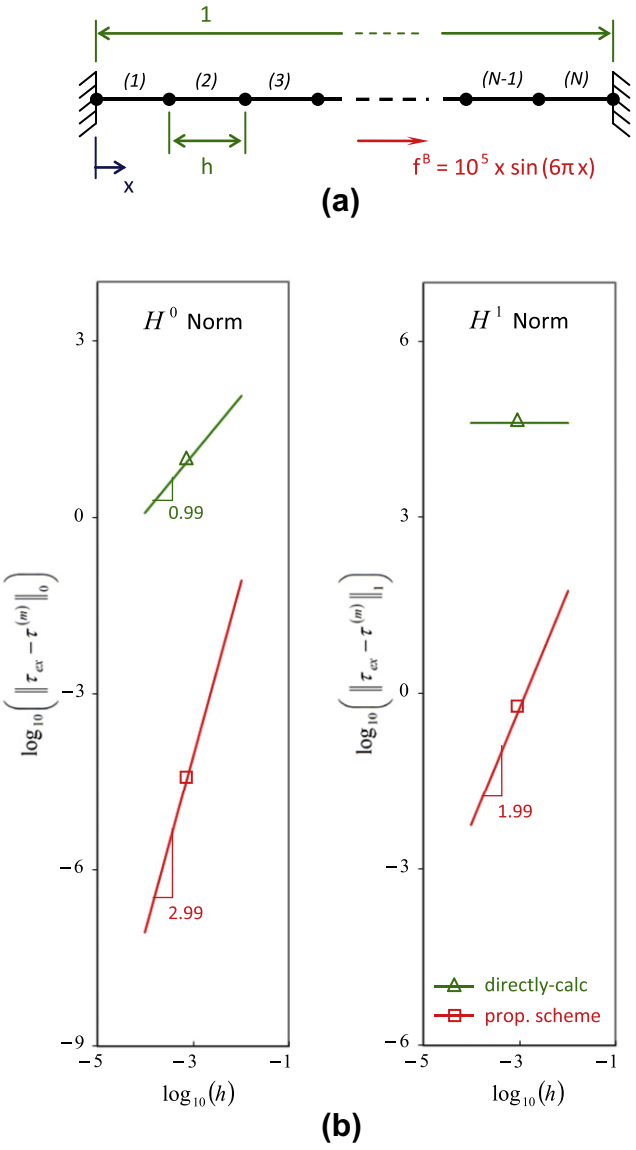

Fig. 3. Ad-hoc test problem to assess the performance of the proposed scheme in 1D solutions ($E = 110 \times 10^9$, $A = 1 \times 10^{-4}$): (a) the test problem and (b) stress convergence curves measured in the Sobolev norm $\|\cdot\|_k$ of order k.

atively, even lower because a step-by-step solution procedure is needed to obtain ${}^t\underline{\widehat{U}}$.

Of course, in practice, the stress calculations need not be performed for the entire assemblage, but instead might be performed only for those elements where stresses should be improved.

4. Insight into the new procedure in 1D solutions

In this section, we first present the solution procedure of the new stress improvement method in 1D settings, then we analyse the method in detail. Thereafter, we compare the performance of the new method with that of the PEM and the REP method.

4.1. Matrices used in 1D solutions

In the following, we consider the 1D case with only one stress component, for arbitrary loading and material properties, and assume that the cross-sectional area of the 1D structure is constant. In this case, an element-based approach is adopted. Hence, to solve

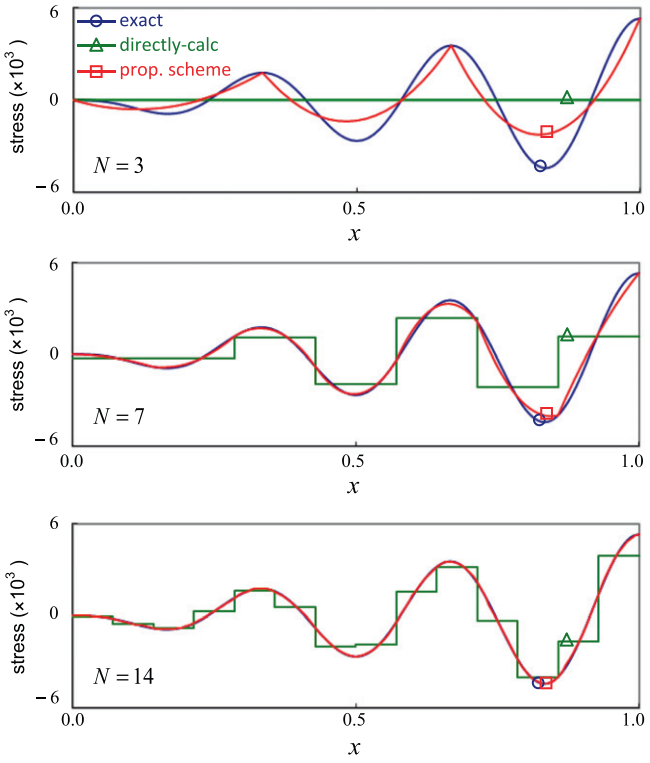

Fig. 4. Stress solutions to the 1D problem defined in Fig. 3a for various different densities of mesh, where N denotes the number of elements used.

for the unknown stress coefficients $\underline{\hat{\tau}}$ for a general element m, we apply Eq. (30) with $N_P = 1$,

$$\underline{E}_\tau = [\,1 \quad x \quad x^2\,], \quad \overline{E}_\tau = [1], \quad \underline{E}_\zeta = [\,1 \quad x\,] \tag{35}$$

and

$$\underline{\partial}_\tau = \left[\frac{d}{dx}\right] \tag{36}$$

where $\underline{\hat{\tau}} = \{\,\alpha_1 \quad \alpha_2 \quad \alpha_3\,\}^T$, and x is the element m local coordinate system.

4.2. Reliability, optimality and convergence of the stress prediction

The fundamental objective of the new procedure is to enhance the accuracy of the stresses. Mathematically, therefore, our goal is to find stresses $\underline{\tau}^{(m)}$ such that

$$\sum_{m=1}^{N} \|\underline{\tau}_{ex} - \underline{\tau}^{(m)}\|_{V^{(m)}} \leqslant c \sum_{m=1}^{N} \left\|\underline{\tau}_{ex} - \underline{\tau}_h^{(m)}\right\|_{V^{(m)}} \tag{37}$$

with a constant $c < 1$, dependent on the problem, and ideally $c \ll 1$.

Here we use the H^1 semi-norm $\|\cdot\|_{V^{(m)}}$ which, when the function in the norm is zero on some part of the boundary, is equivalent to the H^1 norm (by the Poincaré–Friedrichs inequality [1,28]). The semi-norm is appropriate for the stresses because of Eq. (31). We analyse the 1D case considered in Section 4.1 and give details to provide some insight.

In this case, the distance between the exact and the calculated solution is

$$\|\tau_{ex} - \tau^{(m)}\|^2_{V^{(m)}} = \|\tau_{ex}\|^2_{V^{(m)}} + \|\tau^{(m)}\|^2_{V^{(m)}} - 2\left(\int_{V^{(m)}} \left(\frac{d\tau^{(m)}}{dx}\right)\left(\frac{d\tau_{ex}}{dx}\right) dV\right) \tag{38}$$

Because $N_P = 1$, Eq. (32) gives

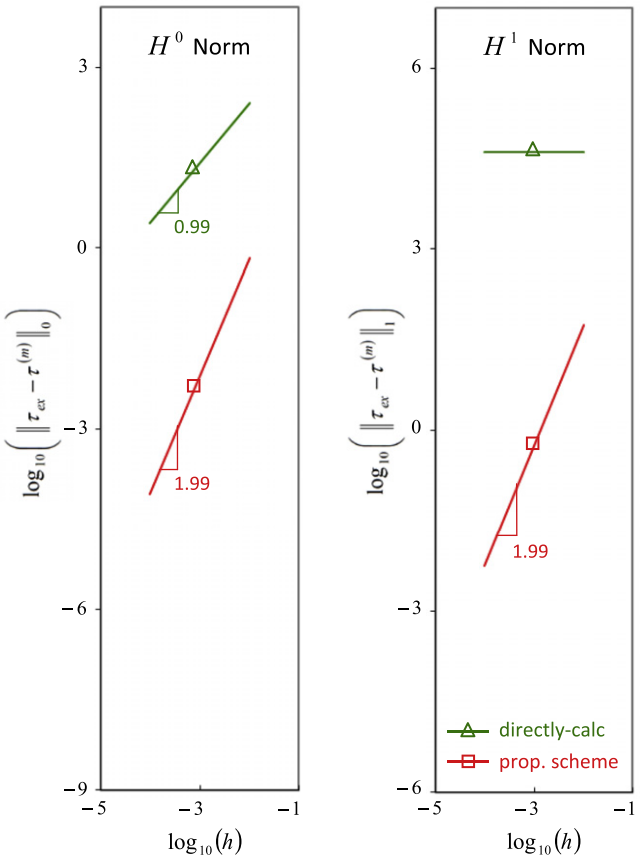

Fig. 5. Stress convergence curves measured in the Sobolev norm $\|\cdot\|_k$ of order k to the 1D problem defined in Fig. 3a, where, in this case, the Young's modulus varies as $E = 110(1 + 0.64\sin(20\pi x)) \times 10^9$.

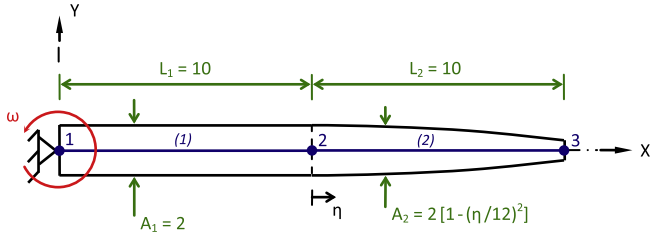

Fig. 6. Rotor blade problem ($E = 110 \times 10^9$, $\rho = 4400$, and $\omega = 10$). The rotor blade spins at a sufficiently high rate that gravitational forces are negligible as compared with the centrifugal forces which act on the blade. The blade is either pinned at node 1 and is free at node 3 ($\widehat{U}_1 = 0$ and $\widehat{U}_3 \neq 0$), or is pinned at node 1 and is welded to a rigid hoop at node 3 ($\widehat{U}_1 = \widehat{U}_3 = 0$).

$$\int_{V^{(m)}} \delta\zeta^{(m)}\left(\frac{d\tau_{ex}}{dx}\right)dV = \int_{V^{(m)}} \delta\zeta^{(m)}\left(\frac{d\tau^{(m)}}{dx}\right)dV$$

for all variations of $\zeta^{(m)} \in P_1$, including when $\delta\zeta^{(m)} = \left(\frac{d\tau^{(m)}}{dx}\right)$. Therefore

$$\int_{V^{(m)}} \left(\frac{d\tau^{(m)}}{dx}\right)\left(\frac{d\tau_{ex}}{dx}\right)dV = \|\tau^{(m)}\|^2_{V^{(m)}}$$

and hence we obtain from Eq. (38) the result

$$\|\tau_{ex}-\tau^{(m)}\|^2_{V^{(m)}} = \|\tau_{ex}\|^2_{V^{(m)}} - \|\tau^{(m)}\|^2_{V^{(m)}} \tag{39}$$

Using the Cauchy–Schwarz inequality [1,28]

$$\|\tau^{(m)}\|^2_{V^{(m)}} \geqslant \frac{1}{V^{(m)}}\left(\int_{V^{(m)}}\left(\frac{d\tau^{(m)}}{dx}\right)dV\right)^2$$

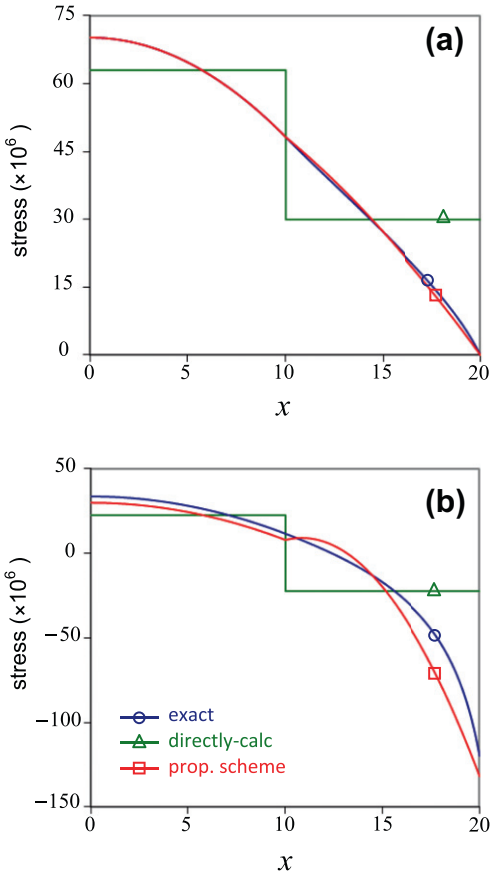

Fig. 7. Stress results for the rotor blade problem defined in Fig. 6: (a) the statically determinate pinned-free case ($\widehat{U}_1 = 0$ and $\widehat{U}_3 \neq 0$) and (b) the statically indeterminate pinned–pinned case ($\widehat{U}_1 = \widehat{U}_3 = 0$).

and the property $\int_{V^{(m)}}\left(\frac{d\tau^{(m)}}{dx}\right)dV = \int_{V^{(m)}}\left(\frac{d\tau_{ex}}{dx}\right)dV$, which follows from Eq. (33), we have

$$\|\tau^{(m)}\|^2_{V^{(m)}} \geqslant \frac{1}{V^{(m)}}\left(\int_{V^{(m)}}\left(\frac{d\tau_{ex}}{dx}\right)dV\right)^2 = \frac{1}{V^{(m)}}\frac{\left(\int_{V^{(m)}}\left(\frac{d\tau_{ex}}{dx}\right)dV\right)^2}{\int_{V^{(m)}}\left(\frac{d\tau_{ex}}{dx}\right)^2 dV}\|\tau_{ex}\|^2_{V^{(m)}} \tag{40}$$

In light of Eqs. (39) and (40), we obtain

$$\|\tau_{ex}-\tau^{(m)}\|^2_{V^{(m)}} \leqslant \left(1 - \frac{1}{V^{(m)}}\frac{\left(\int_{V^{(m)}}\left(\frac{d\tau_{ex}}{dx}\right)dV\right)^2}{\int_{V^{(m)}}\left(\frac{d\tau_{ex}}{dx}\right)^2 dV}\right)\|\tau_{ex}\|^2_{V^{(m)}} \tag{41}$$

Finally, because the displacements vary linearly, then

$$\left\|\tau_{ex}-\tau_h^{(m)}\right\|^2_{V^{(m)}} = \|\tau_{ex}\|^2_{V^{(m)}}$$

and hence we obtain from Eq. (41) the required result

$$\|\tau_{ex}-\tau^{(m)}\|_{V^{(m)}} \leqslant c\left\|\tau_{ex}-\tau_h^{(m)}\right\|_{V^{(m)}} \tag{42}$$

with

$$c = \left(1 - \frac{1}{V^{(m)}}\frac{\left(\int_{V^{(m)}}\left(\frac{d\tau_{ex}}{dx}\right)dV\right)^2}{\int_{V^{(m)}}\left(\frac{d\tau_{ex}}{dx}\right)^2 dV}\right)^{\frac{1}{2}}$$

where $c < 1$. It is interesting to note that if $\tau_{ex} \in P_1$, we have $c = 0$, such that the calculated stresses are exact (when measured in the H^1 semi-norm), *irrespective* of the coarseness of mesh used.

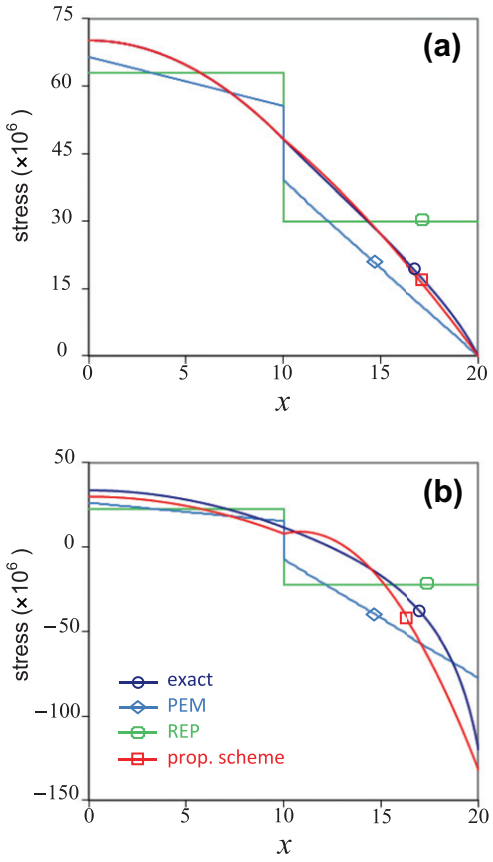

Fig. 8. Stress results for the rotor blade problem defined in Fig. 6: (a) the statically determinate pinned-free case ($\hat{U}_1 = 0$ and $\hat{U}_3 \neq 0$) and (b) the statically indeterminate pinned–pinned case ($\hat{U}_1 = \hat{U}_3 = 0$). The PEM assumes a linear stress, the REP method assumes a constant stress, and the proposed scheme assumes a quadratic stress in each element domain.

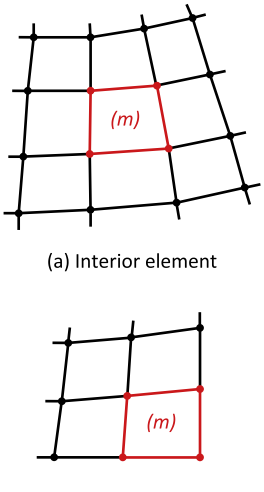

Fig. 9. Stress calculation domain used to solve for the unknown stress coefficients $\underline{\hat{\tau}}$ for a general 2D 4-node element m.

Eq. (42) proves the new method satisfies the fundamental requirement in Eq. (37) for each element, as well as for the entire domain. Also, because $\tau_h^{(m)}$ is stable and converging in the norm [1,10], Eq. (42) proves the method is reliable in 1D solutions and the stresses (within each element) are always more accurate than $\tau_h^{(m)}$ when measured in the norm used.

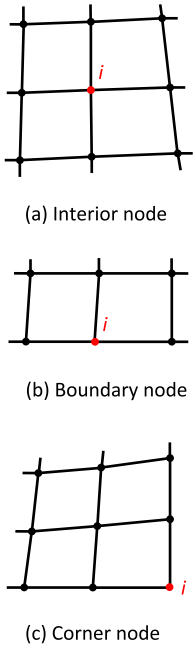

Fig. 10. Stress calculation domain used to solve for the unknown stress coefficients $\underline{\hat{\tau}}$ at a specific node i for a 2D 4-node element mesh.

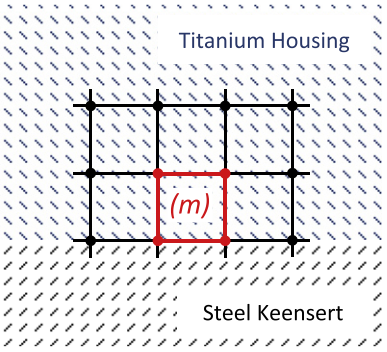

Fig. 11. Stress calculation domain for a general 2D 4-node element m between a titanium housing and a steel Keensert. Element m belongs to the titanium housing group of elements. Since the steel Keensert elements are not included in the stress domain, there is no smoothing across the material discontinuity.

Furthermore, it can be proved (following the usual procedures [1]) that the new method chooses $\tau^{(m)}$ so as to minimise the error within the volume of *each* element m, i.e. $\tau^{(m)}$ is, in fact, the optimal stress prediction,

$$\|\tau_{ex} - \tau^{(m)}\|_{V^{(m)}} \leqslant \|\tau_{ex} - \tilde{\tau}^{(m)}\|_{V^{(m)}} \quad \forall \tilde{\tau}^{(m)} \in P_2 \tag{43}$$

and using interpolation theory on $\tau^{(m)}$ with the result given in Eq. (43), it can also be proved that

$$\sum_{m=1}^{N} \|\tau_{ex} - \tau^{(m)}\|_{V^{(m)}} \leqslant ch^2 \tag{44}$$

where the constant c is independent of h, but depends on the exact solution τ_{ex}.

Therefore, $\tau^{(m)}$ converges to the exact theory of elasticity solution with order $O(h^2)$ in the H^1 norm. In problems where the nodal point displacements are the exact displacements (e.g in Fig. 3), we indeed observed that $\tau^{(m)}$ converges at $O(h^3)$ in the H^0 norm. However, if the nodal point displacements are not the exact displacements, the accuracy of $\tau^{(m)}$ is limited by that of $u^{(m)}$; hence, the

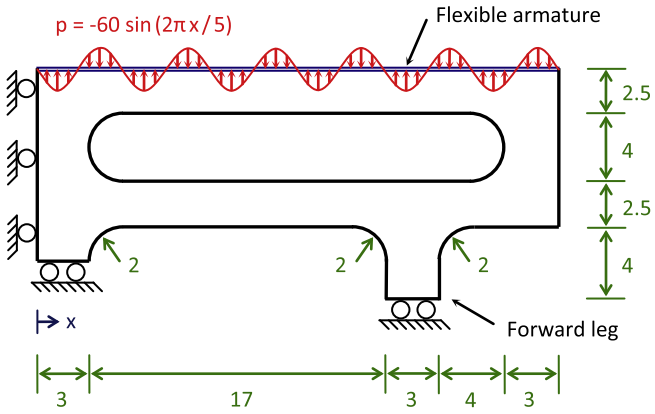

Fig. 12. Actuator subjected to pressure loading problem ($E = 72 \times 10^3$, $\upsilon = 0.3$, thickness = 1, plane stress conditions). The pressure loading is produced by passing current through the armature in the presence of a magnetic field.

highest order of convergence of $\tau^{(m)}$ that we can expect is $O(h^2)$ when measured in the H^0 norm.

Of course, these derivations represent theoretical results; however, experience shows this indeed closely represents the actual behaviour of the discretisations. Figs. 3 and 4 shows the results of an application in which the nodal point displacements are the exact displacements; see Ref. [1]. In Fig. 3, we see that the order of convergence of the enhanced stress is 2.99 in the H^0 norm and 1.99 in the H^1 norm, which compares well with the theoretical result. We further observe in Fig. 4 that when $N = 3$, the directly-calculated stress is zero at every point in the domain (as discussed by Grätsch and Bathe [4] and Hiller and Bathe [16]), but the enhanced stress is still quite reasonable.

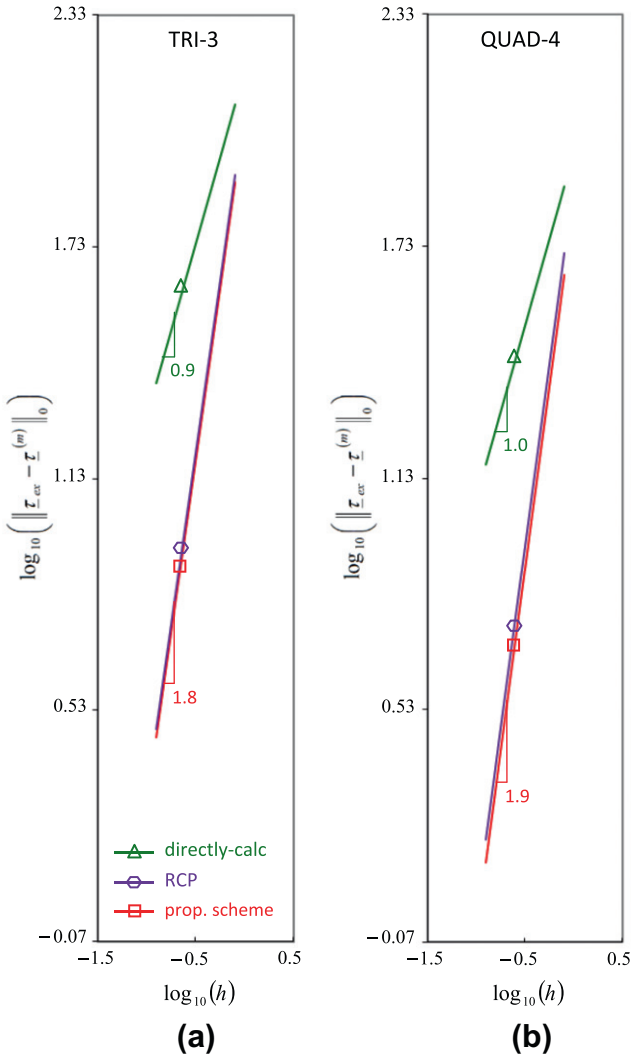

Fig. 13. Stress convergence curves for the actuator problem defined in Fig. 12, measured in the H^0 norm for: (a) the 3-node triangular and (b) the 4-node quadrilateral element.

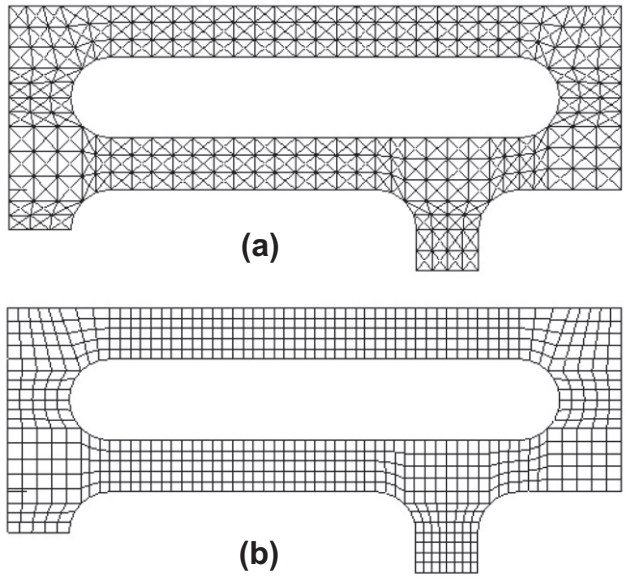

Fig. 14. Starting meshes for the stress convergence curves given in Fig. 13: (a) the 3-node triangular and (b) the 4-node quadrilateral element.

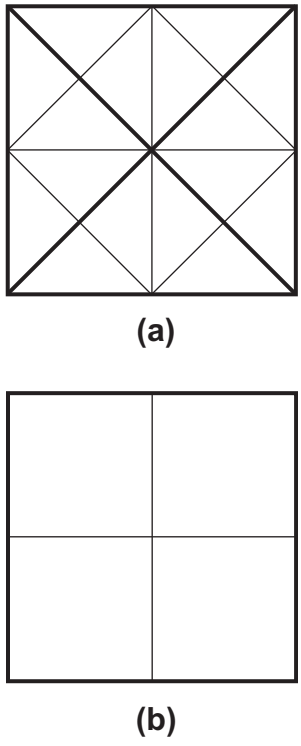

Fig. 15. Refinement sequence used in stress convergence studies. The thick lines depict the initial mesh and the thinner lines depict the next (refined) mesh in the sequence for: (a) the 3-node triangular and (b) the 4-node quadrilateral element.

Fig. 5 shows the results of an application in which the nodal point displacements are not the exact displacements. As expected, in this case, $\tau^{(m)}$ converges at $O(h^2)$ in the H^0 norm, the same as for $u^{(m)}$, but one order higher than that observed for $\tau_h^{(m)}$.

4.3. Numerical example: a rotor blade problem

To illustrate the effectiveness of the new procedure, the response of a rotor blade is studied. Fig. 6 defines the problem. The inboard end of the rotor blade is driven at a constant angular velocity ω; the outboard end is either left free or is welded to a rigid hoop. The rotor blade is idealised as an assemblage of two 2-node truss elements, and the problem is solved using both the usual displacement-based method and the proposed scheme.

We note that in this problem one element has a constant cross-sectional area whereby the other element has a varying area, as shown in Fig. 6. The varying area enters in the equilibrium equation, so that Eq. (15) becomes

$$\int_{L^{(m)}} \delta\zeta^{(m)T}\left\{\frac{d}{dx}(A(x)\tau^{(m)}) + A(x)f_x^B\right\}dx = 0$$

where $L^{(m)}$ and $A(x)$ are the length and cross-sectional area of element m, respectively, and the area is a function of x.

Fig. 7 shows the stress results. In Fig. 7 (and in all other figures), "exact" refers to the exact analytical (or a very accurate numerical) solution of the mathematical model, "directly-calc" refers to the directly-calculated finite element stresses, and "prop. scheme" refers to the finite element stresses predicted using the proposed stress improvement scheme.

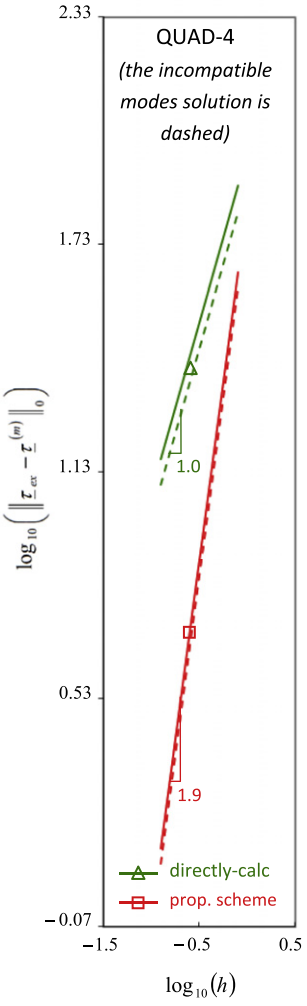

Fig. 16. Stress convergence curves for the actuator problem defined in Fig. 12, measured in the H^0 norm, for the 4-node quadrilateral element with (dashed line) and without incompatible modes (solid line).

Considering the results, we see that the enhanced solution for the stress is significantly more accurate than given directly by the displacements. We further observe that the gradient of the enhanced stress is exact at every point in element 1. Indeed, this will always be the case when the exact stress varies quadratically across the element domain; see Eq. (43).

Next, the rotor blade problem is solved using the PEM [17] and the improved REP method [22]. Typically, the PEM is used to calculate improved interelement tractions for the purposes of error estimation; however, in our comparison the governing equations of the PEM are used to calculate improved stresses.

Fig. 8 shows the stress results, where, for consistency, all methods use only one element in the stress calculation domain. We see that the new procedure performs best. This is expected because the new procedure uses a stress with a higher degree of interpolation than can be used with the other methods, and (most importantly) the solution of the new procedure satisfies the properties discussed in Section 3.6.1. Also, the assumptions employed in the PEM and the REP method limit the accuracy of the results; see Refs. [17,22] and the earlier discussion in Section 1.

Lastly, we note that when $\underline{f}^B \in P_1$, the solution obtained using the RCP method is similar to that obtained using the new method (see Section 5.4.1); hence, for clarity, we do not consider the RCP results here.

5. Insight into the new procedure in 2D solutions

In this section, we first present the solution procedure of the new stress improvement method in 2D settings for a general element m. Then, we discuss how to establish enhanced stresses at a specific node i and how to deal with discontinuous solutions. Thereafter, we assess the performance of the method in static, dynamic and nonlinear solutions.

Since the performance of the RCP methods exceeds that of the REP method (by a considerable margin) [23], we only compare the stresses of the new procedure with the RCP stresses here.

5.1. Matrices used in 2D solutions

In 2D (and 3D) problems, better results are obtained when multiple elements are used in the stress calculation domain. Hence, to solve for the unknown stress coefficients $\hat{\underline{\tau}}$ for a general element m, we use the union of elements that surrounds (and includes) element m as the stress calculation domain; see Fig. 9. Then, we apply Eq. (30) with

$$\underline{E}_\tau = \left[\begin{array}{cccccc|cccccc|cccccc} 1 & y & z & yz & y^2 & z^2 & 0 & 0 & 0 & 0 & 0 & 0 & 0 & 0 & 0 & 0 & 0 & 0 \\ 0 & 0 & 0 & 0 & 0 & 0 & 1 & y & z & yz & y^2 & z^2 & 0 & 0 & 0 & 0 & 0 & 0 \\ 0 & 0 & 0 & 0 & 0 & 0 & 0 & 0 & 0 & 0 & 0 & 0 & 1 & y & z & yz & y^2 & z^2 \end{array}\right] \tag{45}$$

$$\underline{E}_\tau = \left[\begin{array}{ccc|ccc|ccc|ccc} 1 & 0 & 0 & y & z & 2yz & 0 & 0 & 0 & z^2 & 0 & y^2 \\ 0 & 1 & 0 & 0 & 0 & 0 & y & z & 2yz & 0 & y^2 & z^2 \\ 0 & 0 & 1 & -z & 0 & -z^2 & 0 & -y & -y^2 & 0 & 0 & -2yz \end{array}\right] \tag{46}$$

$$\underline{E}_\zeta = \left[\begin{array}{ccc|ccc} 1 & y & z & 0 & 0 & 0 \\ 0 & 0 & 0 & 1 & y & z \end{array}\right] \tag{47}$$

and

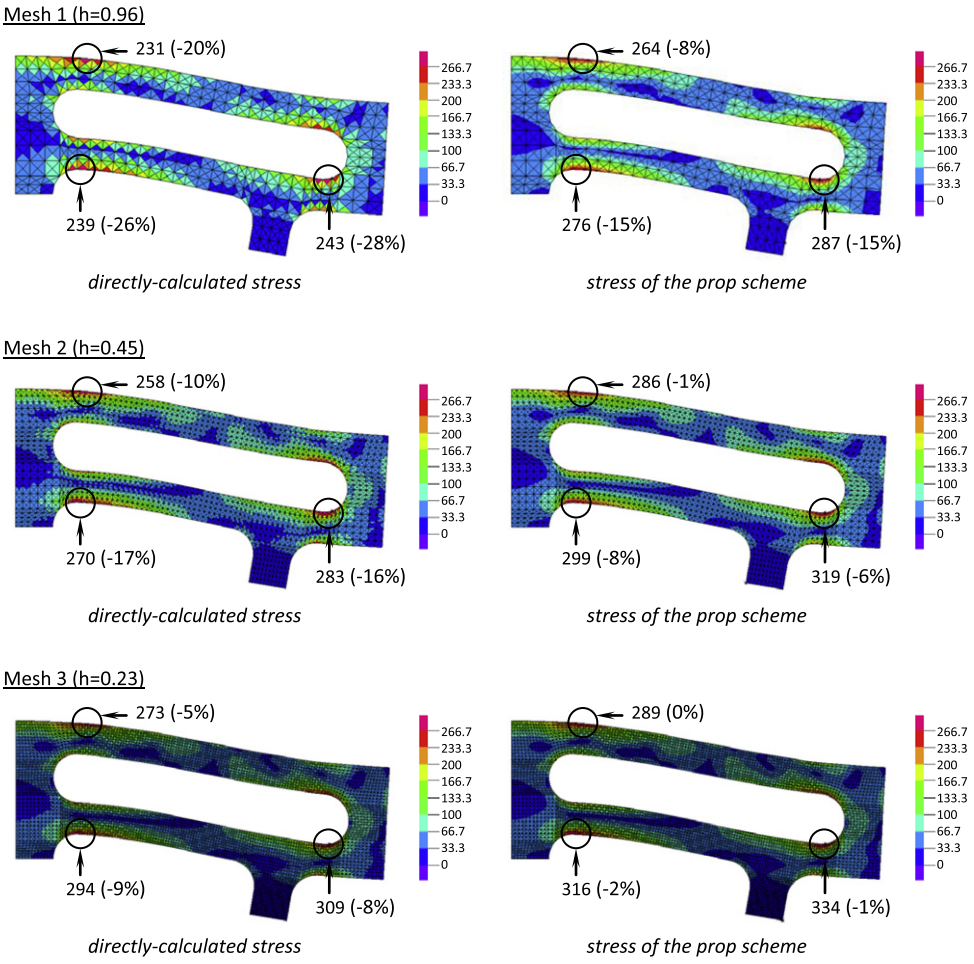

Fig. 17. von Mises stress band plots for the actuator problem defined in Fig. 12, where the forward leg rollers are removed and the material stiffness is reduced by a factor 10. The plate is idealised as an assemblage of 3-node triangular elements. The stress in the band plots is un-averaged (and is shown on the deformed geometry), while the numerical stress values are the averaged nodal point stresses, with the solution error given in parentheses.

$$\underline{\partial}_\tau = \begin{bmatrix} \frac{\partial}{\partial y} & 0 & \frac{\partial}{\partial z} \\ 0 & \frac{\partial}{\partial z} & \frac{\partial}{\partial y} \end{bmatrix} \tag{48}$$

where $\hat{\underline{\tau}} = \{\alpha_1^{yy} \ \cdots \ \alpha_6^{yy} \ \vdots \ \alpha_1^{zz} \ \cdots \ \alpha_6^{zz} \ \vdots \ \alpha_1^{yz} \ \cdots \ \alpha_6^{yz}\}^T$ and (y, z) are the locally based coordinates of the stress calculation domain.

The above description completely defines the stress calculation domain for all types of element and mesh patterns, and no special procedures are needed near the boundaries (nor at the corners) of the mesh. Also, because there is only one possible configuration of stress domain for each element m, the averaging procedure required in Refs. [26,27] is no longer needed.

The RCP method uses the same definition of stress calculation domain [24].

5.2. Solution procedure for a specific node i

For certain problems, we are interested in the stresses at a specific node i, rather than within the element domain. In this situation, we use the union of elements connected to node i as the stress calculation domain. Then, we apply Eq. (30) to solve for the unknown stress coefficients, with the interpolation matrices given in Eqs. (45)–(47).

In the exceptional case where only one element m is connected to node i (e.g. in a corner of the meshed geometry), the elements properly connected to element m should also be included in the stress domain; see Fig. 10.

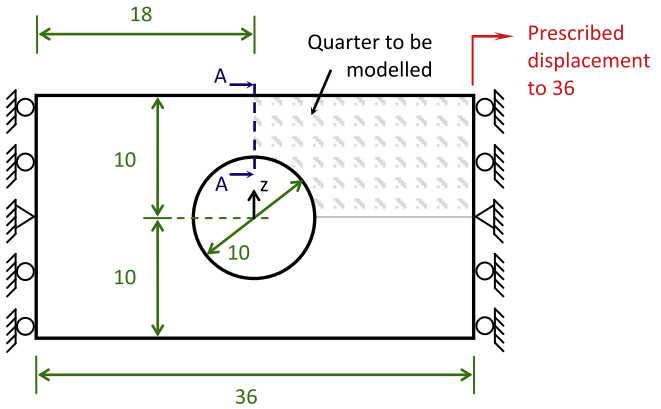

Fig. 18. Large displacement, large strain, rubber plate problem, stretched to 100% of its original length (Ogden material law: $\mu_1 = 0.7$, $\mu_2 = -0.3$, $\mu_3 = 0.01$, $\alpha_1 = 1.8$, $\alpha_2 = -1.6$, $\alpha_3 = 7.5$, $\kappa = 1000$, thickness = 0.5, plane stress conditions). Because of symmetry, only one-quarter of the plate is modelled.

5.3. Dealing with discontinuous solutions

In an actual implementation, the stress calculation domain only contains elements with equal settings. Boundaries between the element groups are treated as free boundaries; see for example

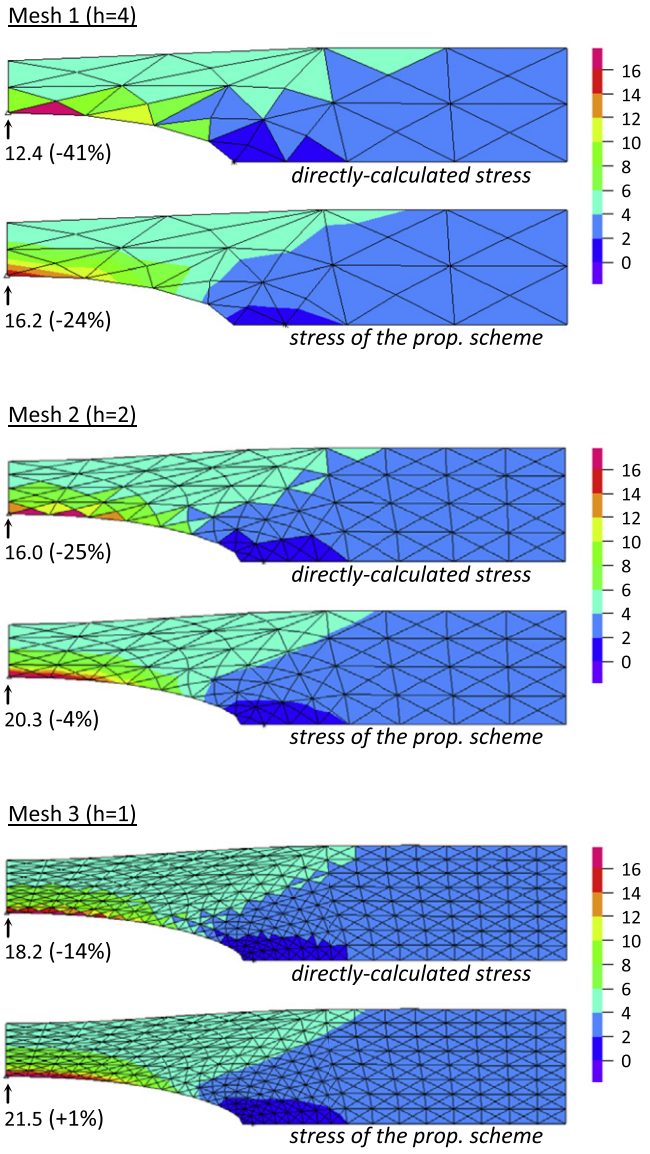

Fig. 19. von Mises stress band plots to the rubber plate problem defined in Fig. 18. The plate is idealised as an assemblage of 3-node triangular elements and the results are shown in the same format as in Fig. 17.

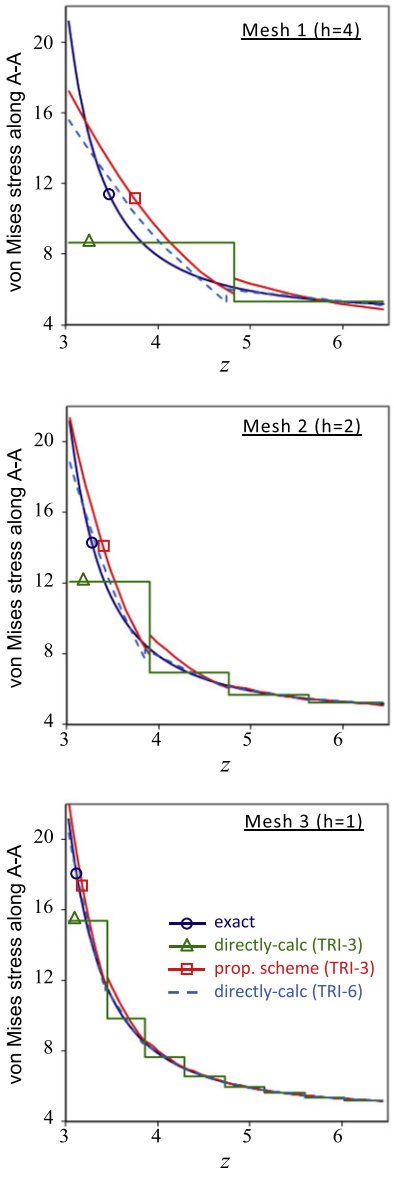

Fig. 20. von Mises stress results along section A–A to the rubber plate problem defined in Fig. 18. The coordinate z references the deformed geometry.

Fig. 11. This prevents the scheme from smoothing discontinuities present in the exact solution.

5.4. Static analysis problems

Two classes of problems are considered: the first where $\underline{f}^B \in P_1$ and the second where $\underline{f}^B \notin P_1$. We show that the new stress improvement method gives good results for both classes of problems, whereas the RCP method only performs well when $\underline{f}^B \in P_1$.

5.4.1. The actuator problem: a case when $\underline{f}^B \in P_1$

The first problem solution involves an actuator subjected to pressure loading. Fig. 12 defines the problem. The problem is statically indeterminate and is solved using both the new method and the RCP method.

Fig. 13 shows the stress convergence curves when a sequence of 3- and 4-node element meshes are used for the solutions. The sequence of meshes is constructed by starting with a mesh of uniform elements of (approximately) equal size, see Fig. 14, then subdividing each element into four equal new elements to obtain the next (refined) mesh in the sequence and so on; see Fig. 15. The mesh size parameter h is calculated by averaging the size of all elements in the assemblage (where the size is taken to be the diameter of a circle which encompasses that element).

Considering the results in Fig. 13, we see that the RCP solution is similar to the solution obtained using the proposed scheme. This will always be the case when $\underline{f}^B \in P_1$ because the quadratically varying stresses are sufficiently rich to satisfy equilibrium for all points in the stress calculation domain; that is, Eq. (27) reduces to Eq. (22) when $\underline{f}^B \in P_1$. However, the solutions are not identical due to the Poisson coupling effects in Eq. (21).

The new procedure can also be used to furnish improved stress predictions for the incompatible modes formulation [1]; see Fig. 16. In these calculations, the unknown stress coefficients are obtained using Eq. (30), where $\underline{\tau}_h^{(m)}$ is established from the incompatible modes solution. This enriches the space implicitly assumed for $\underline{\tau}_h^{(m)}$, but since $\underline{\tau}^{(m)}$ is still assumed to be quadratically interpolated, the solution for $\underline{\tau}^{(m)}$ is similar both with and without incompatible modes.

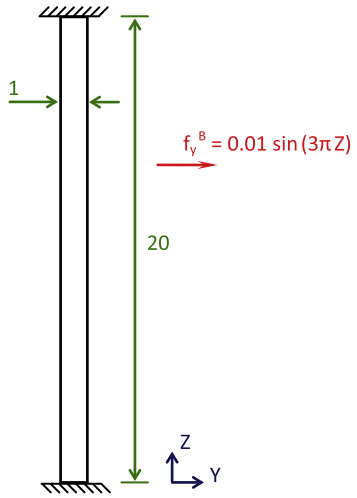

Fig. 21. Armature in a magnetic field problem ($E = 72 \times 10^3$, $\upsilon = 0$, thickness = 1, plane stress conditions). A battery drives constant (direct) current through the armature and the moving charges experience a Lorentz force in the presence of the magnetic field. The Lorentz force is modelled as a body force f_Y^B. We use $\upsilon = 0$ to avoid stress singularities at the four corners.

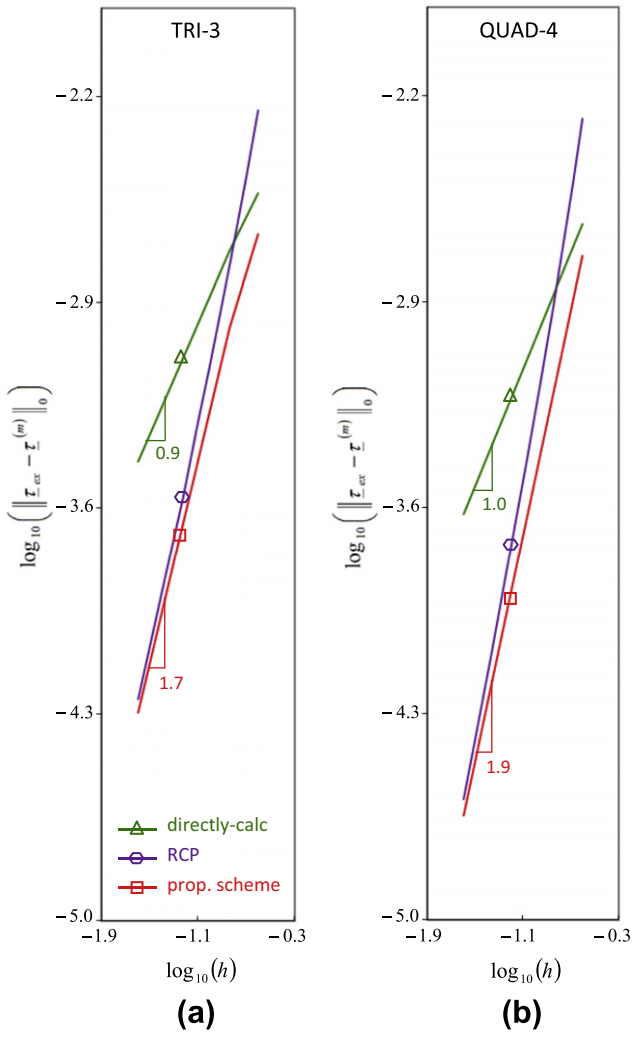

Fig. 22. Stress convergence curves for the armature problem defined in Fig. 21, measured in the H^0 norm for: (a) the 3-node triangular and (b) the 4-node quadrilateral element.

Next, consider the situation where the rollers supporting the forward leg are removed and the material stiffness is reduced by a factor of ten. This requires a large deformation solution. Fig. 17 shows the von Mises stress results for three different meshes (plotted on the deformed geometry). As is clear from this figure, the procedure performs well in the large displacement analysis. Indeed, we see the enhanced stresses, $\underline{\tau}^{(m)}$, are more accurate than the directly-calculated stresses, $\underline{\tau}_h^{(m)}$, even when four times more elements are used to calculate $\underline{\tau}_h^{(m)}$ (i.e. $\underline{\tau}^{(m)}$ of Mesh 1 is more accurate than $\underline{\tau}_h^{(m)}$ of Mesh 2, etc.).

Finally, we solve a large displacement, large strain problem, which includes nonlinear material effects. Fig. 18 defines the problem. The rubber plate is stretched to 100% of its original length by imposing a uniform horizontal displacement at the right end. Figs. 19 and 20 show the von Mises stress results. As expected, the stresses are considerably improved, especially in those regions of high stress gradients, which, of course, is due to the fact that the directly-calculated stresses are constant for the 3-node finite element. Indeed, in Fig. 20, we see that the accuracy of the stresses of the new scheme (calculated using 3-node elements) is comparable to the accuracy of the stresses given directly by the displacements of a 6-node element mesh.

5.4.2. The armature problem: a case when $\underline{f}^B \notin P_1$

In this problem solution, the static response of an armature in a magnetic field is studied. Fig. 21 defines the problem. We wish to establish the stresses in the armature due to the Lorentz force. The problem is solved using both the new method and the RCP method.

Fig. 22 shows the stress convergence curves when a 5×100 starting mesh is used. We see that the new method performs well, but the RCP method gives stresses that are *less* accurate than $\underline{\tau}_h^{(m)}$ for coarse meshes.

The reason that the RCP method gives inaccurate results is that the equilibrium constraint in Eq. (22) is too severe when $\underline{f}^B \notin P_1$. Indeed, to satisfy differential equilibrium, the RCP method uses the following additive decomposition:

$$\underline{\tau}^{(m)} = \underline{\tau}_{h.s.}^{(m)} + \underline{\tau}_{p.s.}^{(m)} \tag{49}$$

where $\underline{\tau}_{h.s.}^{(m)}$ is the unknown homogenous solution of Eq. (22) and $\underline{\tau}_{p.s.}^{(m)}$ is a particular solution of the same equation to be established *a priori* [23,24].

The homogenous solution $\underline{\tau}_{h.s.}^{(m)}$ is assumed to be an element in the subspace of self-equilibrated stresses in P_2, and the unknown stress coefficients in $\underline{\tau}_{h.s.}^{(m)}$ are obtained using Eq. (21),

$$\sum_{m=1}^{N_P}\left(\int_{V^{(m)}} \delta\bar{\underline{\tau}}^{(m)T}\underline{C}^{(m)-1}\underline{\tau}_{h.s.}^{(m)}dV\right) = \sum_{m=1}^{N_P}\left(\int_{V^{(m)}} \delta\bar{\underline{\tau}}^{(m)T}\left\{\underline{\varepsilon}^{(m)} - \underline{C}^{(m)-1}\underline{\tau}_{p.s.}^{(m)}\right\}dV\right) \tag{50}$$

with the particular solution $\underline{\tau}_{p.s.}^{(m)}$ taken as:

$$\underline{\tau}_{p.s.}^{(m)} = \left\{\begin{array}{ccc}\tau_{p.s.}^{yy(m)} & \tau_{p.s.}^{zz(m)} & \tau_{p.s.}^{yz(m)}\end{array}\right\}^T$$

$$\tau_{p.s.}^{yy(m)} = -\int_0^y f_y^B dy, \quad \tau_{p.s.}^{zz(m)} = -\int_0^z f_z^B dz, \quad \tau_{p.s.}^{yz(m)} = 0$$

Therefore, the dimension of $\underline{\tau}_{p.s.}^{(m)}$ depends on $\underline{f}^B$ and the components in Eq. (49) are mismatched when $\underline{f}^B \notin P_1$. As a result, the RCP method is unreliable when $\underline{f}^B \notin P_1$ – e.g. in problems with electromagnetic forces, piezoelectric forces [36], etc. – and gives inaccurate results.

5.5. Dynamic analysis problems

Our objective in this section is to assess the performance of the new method and the RCP method in solving dynamic analysis

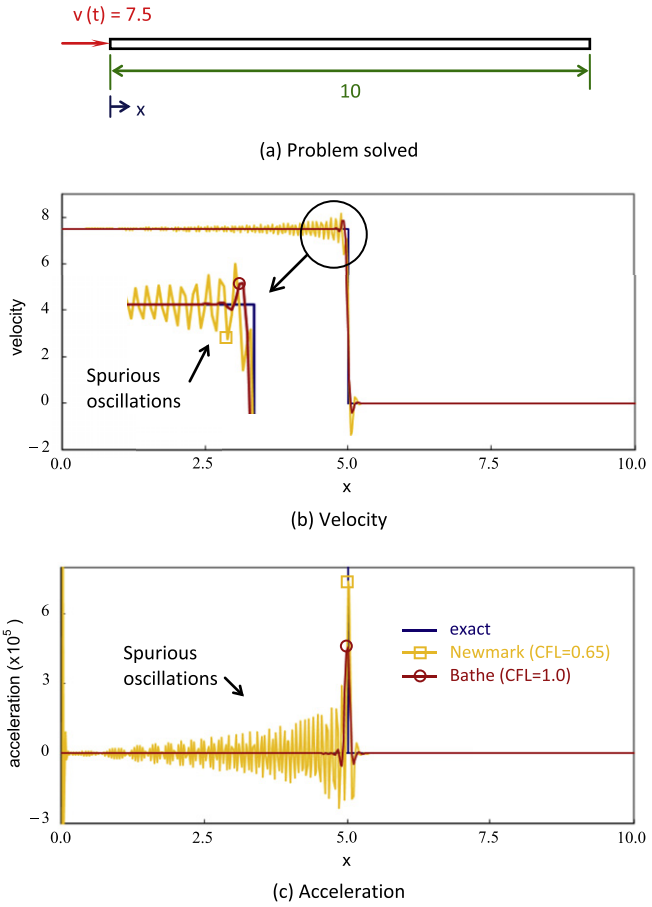

Fig. 23. Impact of an elastic bar ($E = 200 \times 10^9$, $\rho = 8000$, $A = 1$). The bar is initially at rest and the response at time $t = 1 \times 10^{-3}$ is sought. During this time the wave propagates to $x = 5$, there are no reflections. The bar is idealised as an assemblage of 1D 2-node elements of size $h = 0.025$ (400 elements). We give the best results obtained using the Newmark method and the Bathe method when changing for each method the time step size (i.e. the CFL number).

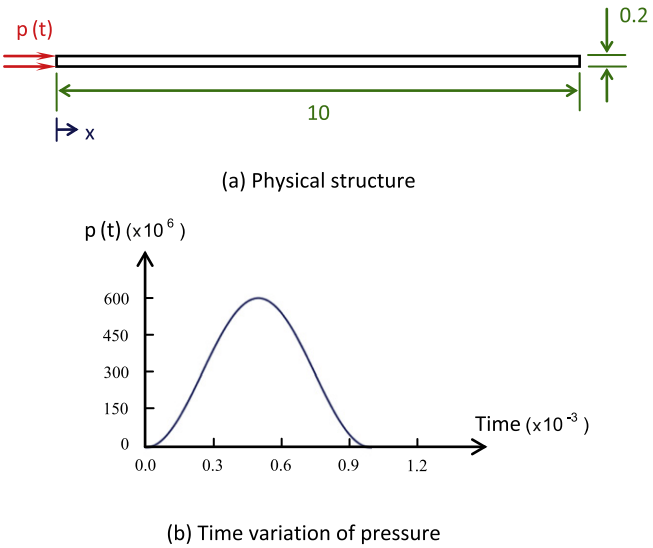

Fig. 24. Propagation of a wave in an elastic bar problem ($E = 200 \times 10^9$, $\rho = 8000$, $\upsilon = 0$, thickness = 0.2, plane stress conditions). The bar is initially at rest and is subjected to a sudden pressure load at one end. The response at time $t = 1.3 \times 10^{-3}$ is sought. During this time the wave propagates to $x = 6.5$, there are no reflections.

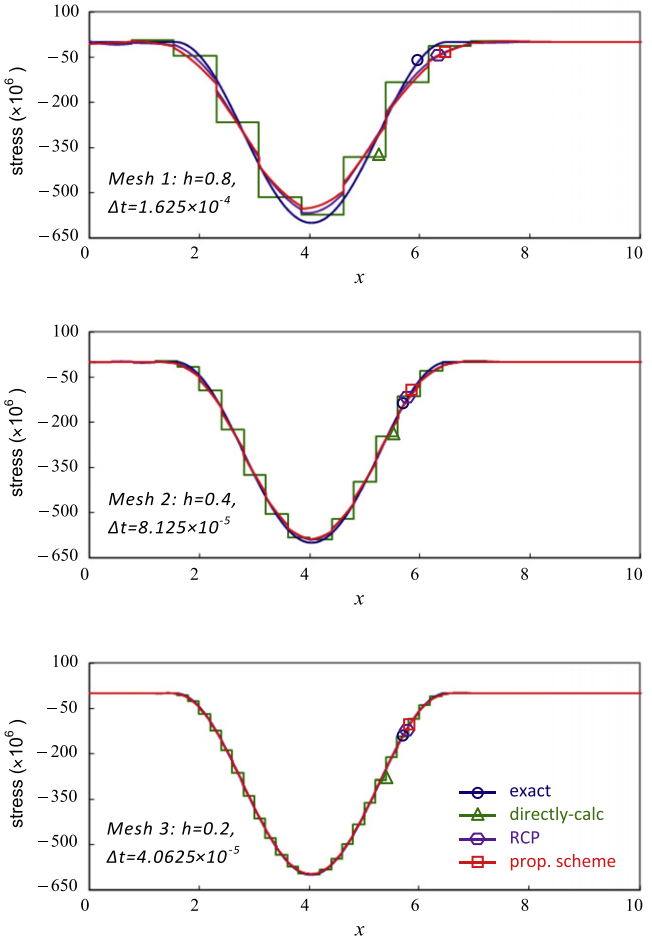

Fig. 25. Longitudinal stress results at $t = 1.3 \times 10^{-3}$ to the wave propagation problem defined in Fig. 24. The bar is idealised as an assemblage of regular 4-node quadrilateral elements, where h denotes the element size and Δt is the time step used. In each case, CFL number = 1.

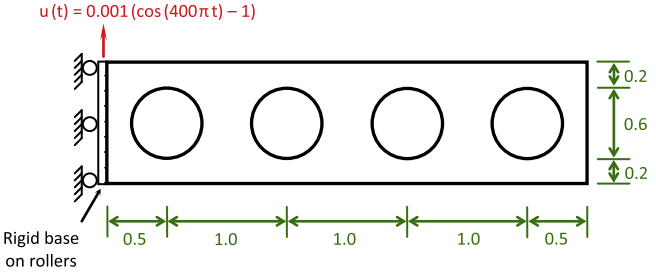

Fig. 26. Lightweight cantilevered plate subjected to base excitation problem ($E = 200 \times 10^9$, $\rho = 7800$, $\upsilon = 0$, thickness = 1, plane stress conditions). The plate is initially at rest and the response at $t = 0.01902$ is sought. No physical damping is introduced in the model. The base of the plate is rigid and the enforced displacement dynamically excites the first eight natural modes of the plate. We use $\upsilon = 0$ to avoid stress singularities at the two corners of the built-in end.

problems. We show that the new method performs well in dynamic analysis and can be used for distorted isoparametric elements, whereas the RCP method can only be used if the elements in the assemblage are un-distorted.

5.5.1. Solution procedure

Stress calculations in dynamics are performed as those in statics, except now the d'Alembert inertia forces are included in $\underline{f}^B$. That is, to obtain the stress coefficients ${}^t\underline{\hat{\tau}}$ of the new method at time t, we use

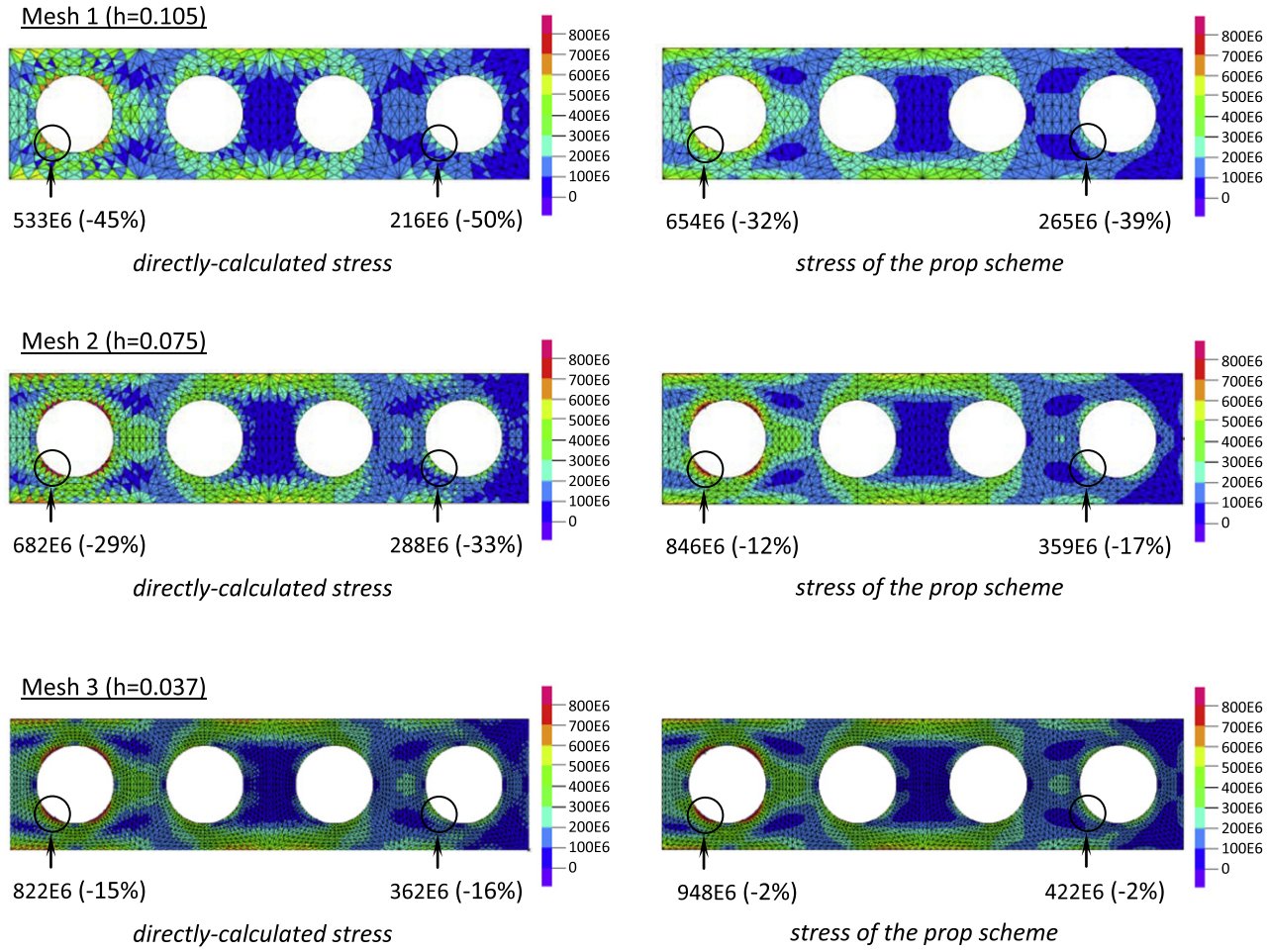

Fig. 27. von Mises stress band plots at $t = 0.01902$ to the lightweight cantilevered plate problem defined in Fig. 26, using 152 time steps. The plate is idealised as an assemblage of 3-node triangular elements. The results are shown in the same format as in Fig. 17.

$$\left[\sum_{m=1}^{N_p}\begin{pmatrix}\int_{V^{(m)}}\overline{\underline{E}}_\tau^T\,\underline{E}_\tau dV\\ \int_{V^{(m)}}\underline{E}_\zeta^T\,\underline{\partial}_\tau\underline{E}_\tau dV\end{pmatrix}\right]{}^t\underline{\hat{\tau}} = \left\{\sum_{m=1}^{N_p}\begin{pmatrix}\int_{V^{(m)}}\overline{\underline{E}}_\tau^T\,{}^t\underline{\tau}_h^{(m)}dV\\ \int_{V^{(m)}}\underline{E}_\zeta^T\{\rho^{(m)}\underline{H}^{(m)}\,{}^t\ddot{\underline{U}}-{}^t\underline{f}^B\}dV\end{pmatrix}\right\} \tag{51}$$

where $\rho^{(m)}$ is the mass density of element m, ${}^t\ddot{\underline{U}}$ lists the nodal point accelerations (i.e. the second time derivative of ${}^t\underline{\hat{U}}$), and the nodal solutions are established using a time integration scheme [1]. In our examples, we use the Bathe implicit time integration procedure because spurious oscillations are very small [37,38]. Fig. 23 gives an example solution where, for the mesh used, we give the best results obtained by the Newmark method (trapezoidal rule) and the Bathe method when changing for each method the time step size (i.e. the CFL number).

To obtain the RCP stresses, we use Eqs. (49) and (50), with the particular solution taken as:

$${}^t\underline{\tau}_{p.s.}^{(m)} = \left\{\begin{matrix}{}^t\tau_{p.s.}^{yy(m)} & {}^t\tau_{p.s.}^{zz(m)} & {}^t\tau_{p.s.}^{yz(m)}\end{matrix}\right\}^T$$

$${}^t\tau_{p.s.}^{yy(m)} = \int_0^y\left(\rho^{(m)}\,{}^t\ddot{u}_y^{(m)} - {}^tf_y^B\right)dy,\quad {}^t\tau_{p.s.}^{zz(m)} = \int_0^z\left(\rho^{(m)}\,{}^t\ddot{u}_z^{(m)} - {}^tf_z^B\right)dz,\quad {}^t\tau_{p.s.}^{yz(m)} = 0$$

where ${}^t\ddot{\underline{u}}^{(m)} = \left[{}^t\ddot{u}_y^{(m)}, {}^t\ddot{u}_z^{(m)}\right]^T = \underline{H}^{(m)}\,{}^t\ddot{\underline{U}}$. However, establishing this particular solution for distorted isoparametric elements is difficult and is an outstanding issue to be solved.

5.5.2. Numerical examples

The first problem solution involves the propagation response of a wave in an elastic bar. Fig. 24 defines the problem. While solved using 2D meshes, due to the geometry and the material definition, this is effectively a 1D wave solution. The problem is solved using both the new method and the RCP method.

Fig. 25 shows the stress results at time $t = 0.001284$; as is clear from this figure, both the new method and the RCP method gives good results.

We note that if spurious oscillations are present in the calculated response, the new method outperforms the RCP method. The reason is that the point-wise equilibrium constraint in Eq. (22) is too severe when the calculated accelerations vary significantly over the stress calculation domain.

In the second problem solution, a lightweight cantilevered plate subjected to base excitation is studied. Fig. 26 defines the problem. The problem is solved using the new procedure. The RCP method cannot be used, since the elements in the assemblage are distorted.

Figs. 27 and 28, respectively, show the von Mises band plots and the stress convergence curves at time $t = 0.01902$. We see that the enhanced stresses are significantly more accurate than the directly-calculated values, both for the 3-node triangular and the 4-node quadrilateral element, and converge at order $O(h^2)$.

6. Concluding remarks

The objective of this paper was to present a general stress improvement procedure that can be used in static, dynamic and nonlinear solutions. We focused the development on the use of low-order displacement-based elements.

First, we showed that the PEM and the REP, RCP and the NPF-based methods [17–27] can all be derived from (or be related to)

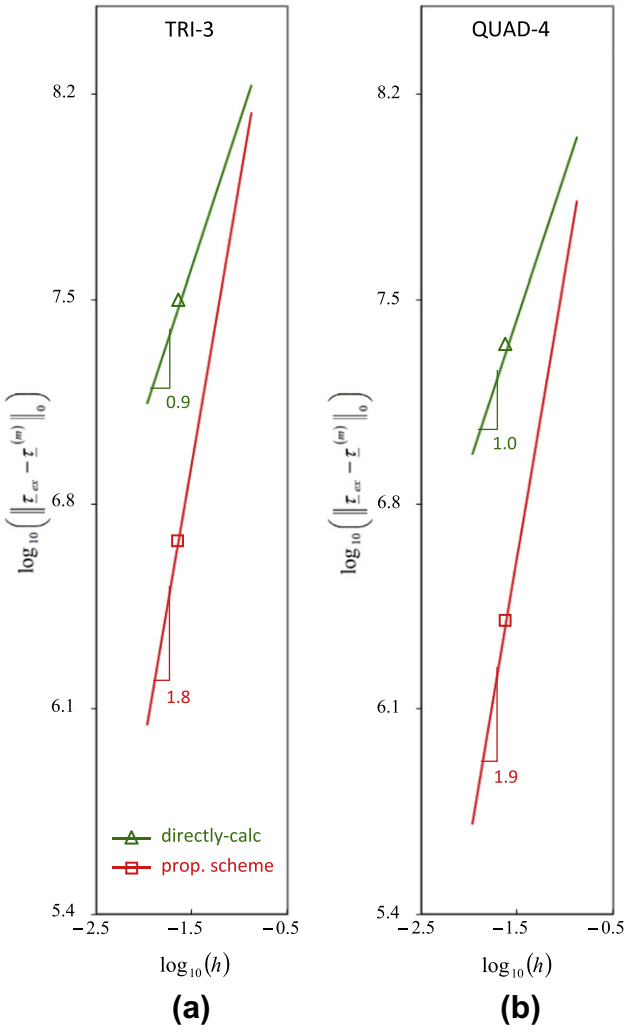

Fig. 28. Stress convergence curves at $t = 0.01902$ for the lightweight cantilevered plate problem defined in Fig. 26, using 152 time steps, measured in the H^0 norm for: (a) the 3-node triangular and (b) the 4-node quadrilateral element.

a mixed formulation based on the Hu-Washizu principle, where the stress–strain relationship is point-wise relaxed but the fulfilment of equilibrium is enhanced.

This mixed variational formulation gives insight, which we used to develop a new stress improvement scheme.

For 1D problems with arbitrary loading and material properties (but constant cross-sectional area), we proved that the new stress improvement scheme is reliable, giving stresses that are, in fact, optimal stress predictions (in the norm used), with the order of convergence being quadratic, i.e. with the same order as the displacements. This convergence behaviour was also seen numerically in 1D and 2D solutions. Indeed, we obtained excellent numerical results for the 1D and 2D problems solved, with the predicted stresses converging quadratically and with a significant downward shift.

While only 1D and 2D solutions are considered here, in linear and nonlinear analyses, the proposed method is directly applicable to 3D solutions in an analogous way and similar results can be expected.

Regarding future research, the use of the new stress improvement procedure might be explored in shell analyses [28], in the solution of multiphysics problems, as well as to establish solution error estimates [3,4].

References

[1] Bathe KJ. Finite element procedures. Cambridge, MA: Klaus-Jürgen Bathe; 2006.
[2] Lo SH, Lee CK. On using different recovery procedures for the construction of smoothed stress in finite element method. Int J Numer Meth Eng 1998;43:1223–52.
[3] Ainsworth M, Oden JT. A posteriori error estimation in finite element analysis. John Wiley; 2000.
[4] Grätsch T, Bathe KJ. A posteriori error estimation techniques in practical finite element analysis. Comput Struct 2005;83:235–65.
[5] Hinton E, Campbell JS. Local and global smoothing of discontinuous finite element functions using a least squares method. Int J Numer Meth Eng 1974;8:461–80.
[6] Bramble JH, Schatz AH. Higher order local accuracy by averaging in the finite element method. Math Comput 1977;31:94–111.
[7] Oden JT, Brauchli HJ. On the calculation of consistent stress distributions in finite element approximations. Int J Numer Meth Eng 1971;3:317–25.
[8] Sussman T, Bathe KJ. Studies of finite element procedures – on mesh selection. Comput Struct 1985;21:257–64.
[9] Sussman T, Bathe KJ. Studies of finite element procedures – stress band plots and the evaluation of finite element meshes. Eng Comput 1986;3:178–91.
[10] Bucalem ML, Bathe KJ. The mechanics of solids and structures – hierarchical modeling and the finite element solution. Springer; 2011.
[11] Zienkiewicz OC, Zhu JZ. The superconvergent patch recovery and a posteriori error estimates Part 1: The recovery technique, Part 2: error estimates and adaptivity. Int J Numer Meth Eng 1992;33:1331–82.
[12] Barlow J. Optimal stress locations in finite element models. Int J Numer Meth Eng 1976;10:243–51.
[13] Blacker T, Belytschko T. Superconvergent patch recovery with equilibrium and conjoint interpol ant enhancements. Int J Numer Meth Eng 1993;36:2703–24.
[14] Wiberg NE, Abdulwahab F, Ziukas S. Enhanced superconvergent patch recovery incorporating equilibrium and boundary conditions. Int J Numer Meth Eng 1994;37:3417–40.
[15] Lee T, Park HC, Lee SW. A superconvergent stress recovery technique with equilibrium constraint. Int J Numer Meth Eng 1997;40:1139–60.
[16] Hiller JF, Bathe KJ. Higher-order-accuracy points in isoparametric finite element analysis and application to error assessment. Comput Struct 2001;79:1275–85.
[17] Stein E, Ohnimus S. Equilibrium method for postprocessing and error estimation in the finite element method. Comput Assist Mech Eng Sci 1997;4:645–66.
[18] Stein E, Ahmad R. On the stress computation in finite element models based upon displacement approximations. Comput Meth Appl Mech Eng 1974;4:81–96.
[19] Stein E, Ahmad R. An equilibrium method for stress calculation using finite element displacement models. Comput Meth Appl Mech Eng 1977;10:175–98.
[20] Ohnimus S, Stein E, Walhorn E. Local error estimates of FEM for displacements and stresses in linear elasticity by solving local Neumann problems. Int J Numer Meth Eng 2001;52:727–46.
[21] Boroomand B, Zienkiewicz OC. Recovery by equilibrium in patches (REP). Int J Numer Meth Eng 1997;40:137–64.
[22] Boroomand B, Zienkiewicz OC. An improved REP recovery and the effectivity robustness test. Int J Numer Meth Eng 1997;40:3247–77.
[23] Ubertini F. Patch recovery based on complementary energy. Int J Numer Meth Eng 2004;59:1501–38.
[24] Benedetti A, de Miranda S, Ubertini F. A posteriori error estimation based on the superconvergent recovery by compatibility in patches. Int J Numer Meth Eng 2006;67:108–31.
[25] Castellazzi G, de Miranda S, Ubertini F. Adaptivity based on the recovery by compatibility in patches. Finite Elem Anal Des 2010;46:379–90.
[26] Payen DJ, Bathe KJ. The use of nodal point forces to improve element stresses. Comput Struct 2011;89:485–95.
[27] Payen DJ, Bathe KJ. Improved stresses for the 4-node tetrahedral element. Comput Struct 2011;89:1265–73.
[28] Chapelle D, Bathe KJ. The finite element analysis of shells – fundamentals. second ed. Springer; 2011.
[29] Brezzi F, Fortin M. Mixed and hybrid finite element methods. Springer; 1991.
[30] Kardestuncer H, Norrie DH. Finite element handbook. McGraw-Hill; 1987.
[31] Brezzi F, Bathe KJ. A discourse on the stability conditions for mixed finite element formulations. J Comput Meth Appl Mech Eng 1990;82:27–57.
[32] Bathe KJ. The inf–sup condition and its evaluation for mixed finite element methods. Comput Struct 2001;79:243–52.
[33] Chapelle D, Bathe KJ. On the ellipticity condition for model-parameter dependent mixed formulations. Comput Struct 2010;88:581–7.
[34] Bathe KJ, Lee PS. Measuring the convergence behavior of shell analysis schemes. Comput Struct 2011;89:285–301.
[35] Mota A, Abel JF. On mixed finite element formulations and stress recovery techniques. Int J Numer Meth Eng 2000;47:191–204.
[36] Benjeddou A. Advances in piezoelectric finite element modeling of adaptive structural elements: a survey. Comput Struct 2000;76:347–63.
[37] Bathe KJ. Conserving energy and momentum in nonlinear dynamics: a simple implicit time integration scheme. Comput Struct 2007;85:437–45.
[38] Bathe KJ, Noh G. Insight into an implicit time integration scheme for structural dynamics. Comput Struct 2012;98–99:1–6.